

To appear in *ApJ*, March 1, 1997, Vol. 477

Detailed Analysis of the Cross-Correlation Function between the X-Ray Background and Foreground Galaxies

Alexandre Refregier¹ and David J. Helfand

Columbia Astrophysics Laboratory, 538 W. 120th Street, New York, NY 10027
email:refreg@odyssey.phys.columbia.edu,djh@carmen.phys.columbia.edu

and

Richard G. McMahon

Institute of Astronomy, Madingley Road, Cambridge CB3 0HA, UK
email:rgm@mail.ast.cam.ac.uk

ABSTRACT

Recent ROSAT surveys suggest that galaxies can constitute the new class of faint sources required to explain the full phenomenology of the cosmic X-Ray Background (XRB). To test this hypothesis without resorting to optical identifications, we compute the two-point cross-correlation function (CCF) estimator $W_{xg}(\theta)$ between 62 *Einstein*-IPC fields (.81-3.5 keV) and the APM Northern galaxy catalog ($13.5 < E < 19.0$). At zero-lag ($\theta = 0$), we detect a 3.5σ correlation signal with an amplitude of $W_{xg}(0) = .045 \pm .013$. This signal passes a series of control tests. At non-zero lag ($\theta > 0$), the angular dependence of W_{xg} has two main features: the main signal for $\theta \lesssim 4'$, and an almost flat plateau with an amplitude of $W_{xg}(\theta \gtrsim 4') \simeq .015$. When fields with galaxy clusters as *Einstein* targets are removed, the plateau virtually disappears, and the zero-lag amplitude becomes $W_{xg}(0) = .029 \pm .013$. We develop a simple, 2-dimensional formalism to interpret the CCF which takes into account the point-spread function of the imaging X-ray detector. Three distinct effects can produce a correlation signal: the X-ray emission from galaxy themselves, the clustering of galaxies with discrete X-ray sources, and the clustering of galaxies with diffuse X-ray emission. It is likely that the plateau at large angles is due to the last effect through the residual diffuse X-ray emission from clusters of galaxies. We do not detect any significant clustering between discrete X-ray sources and galaxies. Using only the fields with non-cluster targets, we find that the mean X-ray intensity of APM galaxies in the .81-3.5 keV band is $(2.2 \pm 1.1) \times 10^{-6}$ cts s⁻¹ arcmin⁻², corresponding to $1.5 \pm .8\%$ of the XRB intensity. The mean X-ray flux of galaxies with $\langle E \rangle = 17.5 \pm .3$ is then

¹also at the Department of Physics, Columbia University

$(8.1 \pm 4.7) \times 10^{-16}$ ergs s⁻¹ cm⁻². This agrees within 1σ with the X-ray flux expected from earlier direct studies of brighter, nearby galaxies, which were shown to result in a total integrated galaxy contribution to the XRB of about 13%. We discuss how this powerful cross-correlation method can be used to measure the flux of X-ray sources well below the detection limit of X-ray instruments, and, perhaps, to probe otherwise undetectable faint diffuse X-ray emission.

Subject headings: Cosmology: Diffuse Radiation - X-Rays: Galaxies - Galaxies: Statistics - X-Rays: General - Methods: Statistical

1. Introduction

In spite of significant recent progress, the nature of the cosmic X-Ray Background (XRB) remains one of the outstanding puzzles in astrophysics (for reviews, see Fabian & Barcons 1992; Zamorani 1995; De Zotti et al. 1995; Hasinger 1996). The observation of the distortion of the Cosmic Microwave Background spectrum with COBE (Mather et al. 1990) precludes the possibility that the hard XRB ($\epsilon \gtrsim 2$ keV) originates from a homogeneous diffuse hot plasma. The alternative explanation, namely a superposition of discrete sources, is supported, at least in the soft band ($\epsilon \lesssim 2$ keV), by deep ROSAT surveys (Hasinger et al. 1993; Vikhlinin et al. 1995a,b,c) in which about 60% of the XRB is resolved into discrete sources, of which, in turn, about 60% are AGN. However, reconciling the full phenomenology of the soft and hard XRB with known properties of AGN has led to several difficulties (Hasinger 1996). First, no single class of known objects has a spectrum consistent with that of the XRB. Also, the surface density of faint ROSAT sources is higher (Hasinger et al. 1993) than expected from the luminosity function of known AGN (Boyle et al. 1993). In addition, fluctuation analyses with GINGA and HEAO1 (Butcher et al. 1994; Mushotzky & Jahoda 1992) imply more sources in the hard band than expected from the ROSAT deep counts by a factor of 2-3.

New detailed unified AGN models stimulated by recent observations could provide a self-consistent solution (for a review, see Setti & Comastri 1996). Another possibility is that a new class of sources becomes important at low fluxes. It has been recently proposed that galaxies, whose fraction is observed to rise at faint fluxes in optical identifications of deep ROSAT surveys, could constitute this new class (Jones et al. 1995; Carballo et al. 1995; Boyle et al. 1995; Romero-Colmenero et al. 1996; see also Hasinger 1996).

One way to study the contribution of galaxies to the XRB in addition to the time-consuming optical-identifications, is to cross-correlate the XRB intensity with galaxy catalogs. A sensitive statistical measure of the correlation at a given angular lag θ is provided by the two-point cross-correlation function (CCF) $W_{xg}(\theta)$. The $\theta = 0$ value of W_{xg} , or “zero-lag” value, is often used, since, in most cases, most of the signal resides at small angles. However, the full correlation signal is provided by the “non-zero lag” ($\theta > 0$) sector of W_{xg} .

This approach was initiated by Jahoda et al. (1991) who computed W_{xg} at zero lag between 2-10 keV HEA0 1 A-2 maps of the XRB and the UGC and ESO galaxy catalogs. They found a significant correlation signal with an amplitude of $W_{xg}(0) = (3 \pm 1) \times 10^{-3}$, and concluded that as much as 50-70% of the XRB could be due to X-ray sources associated with present-epoch galaxies. Lahav et al. (1993) confirmed the correlation signal by applying the technique to 4-12keV GINGA maps of the XRB compared with the UGC and IRAS galaxy catalogs. However, they pointed out that a correct interpretation of the correlation requires taking source clustering into account. Their revised estimate of the fraction of the XRB due to a non-evolving population of X-ray sources spatially associated with local galaxies is $30 \pm 15\%$. From a careful modelling of the correlation found between the HEA0 1 A-2 maps and the IRAS galaxy catalog, Miyaji et al. (1994) derived a local X-ray emissivity which correspond to about 20% of the XRB without evolution and which can be accounted for by AGN alone (see also Barcons et al. 1995). A similar fraction (10-30%) was obtained by Carrera et al. (1995a,b) from a measurement $W_{xg}(\theta)$ at non-zero lag, between GINGA and several galaxy catalogs.

The aforementioned correlation studies were focused on the hard ($E > 2$ keV) XRB. Because only data from non-imaging X-ray instruments were available in this band, this work was restricted to rather large angular scales ($\theta > 1$ deg). In addition, only catalogs of bright, nearby galaxies were employed. More recently, Roche et al. (1995) detected a correlation signal between ROSAT-PSPC fields and faint galaxies ($B < 23$). The high angular resolution of ROSAT allowed them to probe small angular scales ($\sim 15''$). However, their consideration of only three ROSAT fields limited their statistics. By applying a detailed correlation formalism to the ROSAT results, Treyer & Lahav (1995) concluded that about 22% of the .5-2 keV XRB is due to faint galaxies with $18 < B < 23$.

In order to test these results at intermediate angular scales ($\sim 1'$) and with improved statistics, we have cross-correlated 62 *Einstein*-IPC fields with the APM Northern Galaxy catalog ($13.5 < E < 19$). To extract the full correlation information, we have computed both the zero and non-zero lag CCF. The improved statistics allows us to give a better estimate of the statistical uncertainty in the correlation signal. Several control experiments provide added confidence in the significance of our results. The *Einstein* energy band (.1-3.5 keV) is sufficiently broad for testing the energy dependence of the signal. In addition, we develop a simple, 2-dimensional formalism to interpret the angular dependence of W_{xg} which takes into account the Point Spread Function (PSF) of the imaging X-ray instrument.

This paper is organized as follows. We first describe the X-ray and galaxy data (§2). We then outline our procedure for measuring the correlation function estimator W_{xg} (§3). In §4, we present the zero and non-zero lag results, along with the analysis of the various control samples. We then present our interpretation formalism (§5) and discuss the implications of the detected correlation for the contribution of galaxies to the XRB (§6). The details of the calculations involved in the interpretation of W_{xg} are relegated to appendix A. In appendix B, we explicitly evaluate two multi-dimensional integrals which appear in this interpretation. Finally, a treatment of the statistics of W_{xg} is presented in appendix C. The zero-lag results have already been reported in a

brief form in Refregier et al. (1995).

2. Data

2.1. X-Ray

The original X-ray data consisted of northern ($\text{Dec.} > -5^\circ$) *Einstein* Imaging Proportional Counter (IPC) fields (Giacconi et al. 1979) at high galactic latitude ($|b| > 25^\circ$). We originally selected 77 random fields with typical exposure times greater than 5000 s. We avoided fields containing bright sources and/or large areas of diffuse emission. The mean exposure time was $\langle t_{exp} \rangle \simeq 1.4 \times 10^4$ s. In order to focus on the unresolved component of the XRB, sources were excised down to 3.5σ . This corresponds to a mean excision flux of $\langle S_{exc}(.81 - 3.5\text{keV}) \rangle = (4.8 \pm .5) \times 10^{-14}$ ergs cm^{-2} s^{-1} . The source excision and flat-fielding procedures are described in Hamilton et al. (1991) and Wu et al. (1991). The type of target was recorded for each field and classified into four broad categories (see Table 1): galactic sources, extragalactic discrete sources (galaxies, QSO, etc), clusters (and superclusters) of galaxies, and deep fields. This allowed us, in particular, to study subsamples of fields with and without clusters of galaxies as targets.

The photons in each one-square-degree field were binned into $64''$ pixels. The Point-Spread Function (PSF) for the IPC is close to a gaussian with standard deviation $\sigma_{psf} \simeq .5'$. A typical X-ray field is shown as the grey-scale map in figure 1. The blank region in the $4'$ -wide criss-cross pattern, due to the window support ribs, has been excluded from our analysis. We considered two energy bands: “soft” (.16-.81 keV) and “hard” (.81-3.50 keV). The hard band is to be considered as the data set of interest, whereas the soft band, which is dominated by emission from the Milky Way, is used as a control data set. In general, fields in the *Einstein* archive have different levels of contamination from solar X-rays scattered into the telescope by the residual atmosphere. This is parametrized by the Viewing Geometry (VG) flag with $\text{VG}=1$ ($\text{VG}=3$), corresponding to low (high) contamination. For the real data set, only exposures with relatively low solar contamination ($\text{VG}=1-2$) were considered. Another control data set was constructed by keeping higher solar contaminations ($\text{VG}=2-3$). Even though the low and high contamination data sets both contain $\text{VG}=2$ exposures and thus overlap, they can be compared to test the qualitative dependence of the correlation signal on solar contamination.

For the *Einstein*-IPC, counts result from several effects (Wu et al. 1991). The instrumental background due to cosmic-ray particle contamination and calibration source leakage amounts to $\langle i^{part} + i^{calib} \rangle = (1.1 \pm .1) \times 10^{-4}$ cts s^{-1} arcmin^{-2} . The latter and following intensities correspond to the hard band (.81-3.5 keV) and to the subset of our fields with targets other than galaxy clusters. The solar contamination for $\text{VG} = 2 - 3$ exposures is well described by a bremsstrahlung spectrum with $kT = .25$ keV and produces, on average, about $.19 \times 10^{-4}$ cts s^{-1} arcmin^{-2} (Wang et al. 1991). We thus estimate that, for $\text{VG} = 1 - 2$ exposures, this contribution produces $\langle i^{sol} \rangle = (.1 \pm .1) \times 10^{-4}$ cts s^{-1} arcmin^{-2} . The XRB, including the contribution from the Milky

Way, produces $\langle i^{XRB} \rangle = (1.4 \pm .1) \times 10^{-4}$ cts s⁻¹ arcmin⁻². By integrating the number-flux relation measured by Gioia et al. (1990) in the context of the *Einstein* Medium Sensitivity Survey (EMSS), we estimate that the source excision mentioned above amounts to the removal of an average of $\langle i^{exc} \rangle = (.10 \pm .03) \times 10^{-4}$ cts s⁻¹ arcmin⁻². (We have assumed a mean power law spectrum with index .7 for the sources and $N_H = 3 \times 10^{20}$ cm⁻² to convert from the EMSS band). The final expected count rate is thus $\langle i \rangle \equiv \langle i^{part} + i^{calib} + i^{XRB} - i^{exc} \rangle = (2.5 \pm .3) \times 10^{-4}$ cts s⁻¹ arcmin⁻². For our data set, we measure a mean intensity of $\langle i \rangle = (2.73 \pm .01) \times 10^{-4}$ cts s⁻¹ arcmin⁻², consistent with the expected count rate.

2.2. Galaxies

The APM Northern Catalog (Irwin & McMahon 1992; Irwin et al. 1994) consists of scans of E and O Palomar Observatory Sky Survey (POSS-I) plates by the SERC Automatic Plate Measuring (APM) machine in Cambridge (Kibblewhite et al. 1984). Objects are assigned position coordinates, E and O apparent magnitudes, a morphological class and various morphological parameters. The objects in the raw APM object catalog were classified on the basis of a compactness parameter similar to that used by Maddox et al. (1990b). The morphological classes comprise stars, galaxies, noise and merged objects. The catalog includes objects down to $E \simeq 20$.

In this study, we rejected 10 fields which had abnormal patterns of galaxies due mostly to spurious object detections around bright stars. We only considered the E-plate objects with $13.5 < E < 19$. This choice maximized the performance of the automatic image classifier, and resulted in about 530 galaxies per degree square. In this magnitude range and in our latitude range, the number of stellar objects outnumber galaxies by a factor of about 5. In figure 1, a typical distribution of galaxies in this magnitude range is displayed as filled circles. The positional accuracy of the APM objects is better than one arcsecond. Being much smaller than our pixel size (64''), this uncertainty is negligible in our analysis. In order to avoid potential complications at POSS plate boundaries, we chose the field centers to lie further than 45' from the plate edges. Catalogued stellar objects found in the same fields were used as a control data set.

It is useful to convert E-magnitudes into other magnitude systems. As was summarized by Koo & Kron (1992), the mean colors of galaxies is independent of magnitude for $b_J \lesssim 22$ and is close to $\langle b_J - r_f \rangle_{gal} = 1.1 \pm .1$. Using figures 1 and 4 in Butcher & Oemler (1985), we infer that, for galaxies, $\langle B - R \rangle_{gal} = 1.9 \pm .2$, $\langle B - V \rangle_{gal} = 1.1 \pm .1$, and thus that $\langle V - R \rangle_{gal} = .8 \pm .2$. By measuring the magnitudes of stellar standards with the Automated Plate Scanner, Humphreys et al. (1991) have shown that, for the POSS plates, $E - R \simeq -.011 + .148(V - R) + .058(V - R)^4$, for $-.2 < V - R < 1.7$. Assuming that this relation also holds for the APM measurements, the above colors translate to $\langle E - R \rangle_{gal} = .3 \pm .2$, $\langle V - E \rangle_{gal} = .5 \pm .3$, and $\langle B - E \rangle_{gal} = 1.6 \pm .3$. Finally, figure 9 in Butcher & Oemler (1985), yields $\langle b_J - E \rangle_{gal} = 1.1 \pm .3$.

The mean magnitude of our galaxy sample is given by $\langle E \rangle \equiv \int_{E_{min}}^{E_{max}} dE E \frac{dn}{dE} / \int_{E_{min}}^{E_{max}} dE \frac{dn}{dE}$,

where E_{min} and E_{max} are the magnitude limits of the sample, and $\frac{dn}{dE}$ is the mean number of galaxies per unit solid angle and per unit magnitude. In our sample, $E_{min} = 13.5$ and $E_{max} = 19$, as stated above. A fit to the number-magnitude relation in our sample yields $\log(dn/dE) \simeq -3.44 + .30E$ galaxies deg^{-2} $(.5 \text{ mag})^{-1}$, so that $\langle E \rangle \simeq 17.7$. However, our directly measured number-magnitude relation is flatter than the one measured for the southern APM catalog (Maddox et al. 1990), which after using the above $b_J - E$ conversion is well fitted by $\log(dn/dE) \simeq -8.8 + .6E$ galaxies deg^{-2} $(.5 \text{ mag})^{-1}$, for $E \lesssim 19$. This discrepancy is probably due to a systematic overcorrection for saturation for galaxy magnitudes. (The slope of the stellar APM counts is consistent with the stellar counts of Metcalf et al. 1991). The northern and southern APM counts agree if we use corrected APM magnitudes defined as $E' = 8.52 + .50E$. In this case, our sample limits are $E'_{min} = 15.3$ and $E'_{max} = 18.1$ and the mean magnitude becomes $\langle E' \rangle \simeq 17.4$. Given the uncertainty involved in this correction, we take our mean magnitude to be $\langle E \rangle \simeq 17.5 \pm .3$.

The contamination by misclassified objects in the APM galaxy catalog was estimated at bright magnitudes by direct visualization of 841 objects on five different POSS plates. The stellar contamination was observed to vary from plate to plate and as a function of magnitude, and is dominated by misclassified stars. The mean ratio of the number of true galaxies to the total number of objects classified as galaxies in the APM is $\langle N^g \rangle / \langle N \rangle \simeq .7 \pm .2$ for $15 \lesssim E \lesssim 16.5$ and tends to decrease with magnitude, at least in this magnitude range. Direct visualization for $E \gtrsim 16.5$ is unreliable. Using deeper AAT plates, Maddox et al. (1990b) estimate that, for the southern APM galaxy catalog, $\langle N^g \rangle / \langle N \rangle \simeq .95$, for $17 < b_J < 20$. We thus finally set $\langle N^g \rangle / \langle N \rangle \simeq .8 \pm .2$ as our estimate for magnitudes close to our mean $\langle E \rangle$.

2.3. Final Sample

From the resulting set of 67 fields, we removed overlapping fields giving preference to those with higher exposure times. This was done to avoid correlating the same region of the sky more than once. (Two fields overlapping by less than $15'$ were left in the sample). The final field sample contained $N_f = 62$ fields which were labeled by their *Einstein* sequence numbers. Their center positions along with the associated POSS plate numbers, exposure times, *Einstein* target types, mean X-ray intensities, and mean galaxy surface densities are listed in table 1. Figure 1 shows one of the X-ray fields superimposed on the associated distribution of galaxies.

An additional control data set was generated by scrambling the X-ray/galaxy field pairs. To summarize, we considered the following data sets:

1. Hard-Galaxies: Hard-band (.81-3.5 keV) XRB (low solar contamination) crossed with galaxies: the real data set
2. Hard(Solar)-Galaxies: Hard-band XRB with high solar contamination crossed with galaxies

3. Soft-Galaxies: Soft-band (.16-.81 keV) diffuse emission (with a large Galactic component) crossed with galaxies
4. Hard-Stars: Hard-band XRB crossed with stars
5. Hard-Galaxies (Scrambled): As in set 1, but with scrambled field pairs.

The first data set is the principal (“real”) data set. We should not detect any correlation for the scrambled set (set 5), since it involves pairs of unrelated regions of the sky. As mentioned above, the soft band XRB is dominated by X-rays from the Milky Way. Thus, for data sets 2 and 3, the fraction of the X-ray counts potentially correlated with galaxies is smaller than that for the real set; we therefore expect the correlation to be smaller for these two sets. Stars contribute a non-negligible fraction of the XRB: the fraction of stars optically identified in the *Einstein* Medium Sensitivity Survey (Stocke et al. 1991) and deep ROSAT XRB surveys (see Hasinger 1996, for a summary) are 26% and 15%, respectively. Given the significant (mostly stellar) contamination of the galaxy catalog, it is important to test whether stars contribute to the CCF. This is achieved by the use of data set 4. After binning galaxies (and stars) into $64''$ pixels, the correlation analysis was performed in the same way for the five data sets. This provides a direct and powerful test of the physical and statistical significance of any resulting correlation signal.

3. Procedure

3.1. Correlation Function and Estimator

Our main goal was to estimate the two-point angular cross-correlation function w_{xg} for the two data sets described above. This function is a sensitive measure of correlations between two-dimensional data sets (see eg., Peebles 1980; Jahoda et al. 1991). To define w_{xg} , let us consider two infinitesimal cells C_1 and C_2 with solid angles $\delta\Omega_1$ and $\delta\Omega_2$ with angular separation θ_{12} . Let δN_1 be the number of galaxies in C_1 , and δI_2 be the XRB flux (in ergs $\text{cm}^{-2} \text{s}^{-1}$) in C_2 . Then, w_{xg} is defined by

$$\langle \delta N_1 \delta I_2 \rangle = \langle n \rangle \langle i \rangle [1 + w_{xg}(\theta_{12})] \delta\Omega_1 \delta\Omega_2, \quad (1)$$

where $\langle n \rangle$ is the mean number of galaxies per sr and $\langle i \rangle$ is the mean XRB intensity (in ergs $\text{cm}^{-2} \text{s}^{-1} \text{sr}^{-1}$), and the brackets denote a sky average. By taking $\delta\Omega_1$ to be sufficiently small, one can show that equation (1) implies that $w_{xg}(\theta)$ is the mean fractional excess in the XRB intensity at an angle θ from a given galaxy.

In practice, measurement cells have a finite size and one can not measure w_{xg} directly. Instead, one computes the finite-cell estimator W_{xg} defined as

$$W_{xg}(\theta) \equiv \frac{\eta(\theta)}{\langle N \rangle \langle I \rangle} - 1, \quad (2)$$

where $\langle N \rangle$ and $\langle I \rangle$ are the number of galaxies and the XRB flux averaged over all available cells. The quantity $\eta(\theta)$ in the numerator is defined by

$$\eta(\theta_{12}) \equiv \langle N_1 I_2 \rangle_{\theta_{12}}, \quad (3)$$

where the bracket denotes the product of N and I averaged over cell C_1 and C_2 with an angular separation θ_{12} . (Our data set, which consists of many disjoint fields, was analyzed with the specific averaging scheme described in §3.2.) In general, W_{xg} depends on the cell size α and can thus be thought of as being a function of two variables: $W_{xg} = W_{xg}(\alpha, \theta)$. If the XRB and the galaxy counts are uncorrelated, $\eta(\theta) = \langle N \rangle \langle I \rangle$ and thus $W_{xg} = 0$. On the other hand if they are correlated (anticorrelated) W_{xg} is positive (negative).

Formally, the correlation function w_{xg} is equal to the estimator W_{xg} for infinitely small cell size, i.e.

$$w_{xg}(\theta) = \lim_{\alpha \rightarrow 0} W_{xg}(\alpha, \theta). \quad (4)$$

Conversely, W_{xg} is obtained from w_{xg} as

$$W_{xg}(\alpha, \theta_{12}) = \frac{1}{2\pi\alpha^4} \int d\phi_{12} \int_{C_1} \int_{C_2} d\Omega'_1 d\Omega'_2 w_{xg}(\theta'_{12}), \quad (5)$$

where the $d\Omega'_i$ integrals are over two cells C_1 and C_2 separated by an angle θ_{12} with polar coordinates (θ_{12}, ϕ_{12}) in a coordinate system whose origin is the center of C_1 . The $d\phi_{12}$ integral operates as an average over all possible relative positions of the two cells while keeping their separation θ_{12} constant. We have taken the cells to be squares with sides α . Equation (5) can be derived by subdividing the two cells into infinitesimal subcells and by using equation (1) in equation (2).

3.2. Implementation

In our experiment, our minimal cells are the X-ray pixels: squares with a side length of $\alpha_p = 64''$. The galaxies (and the stars) were also binned into such pixels. All invalid pixels, i.e. pixels under the support ribs or outside the *Einstein* field were ignored. We varied the cell size α by binning adjacent pixels together. Boundary cells, i.e. cells lying across the field edge or across the ribs, were rejected if less than 33% of their area were valid. The choice for this threshold was rather arbitrary and reflected a tradeoff between wasting pixels and having too many cells with large uncertainties. A moderate variation of this threshold (between 20% and 60%) did not affect our results significantly. We thus obtained values of W_{xg} at zero-lag for cell sizes $\alpha = n\alpha_p$, where n is an integer. We only considered one-pixel cells ($\alpha = \alpha_p$) for our non-zero lag measurements.

For each field, we computed $\eta(\theta)$ (Eq. [3]) as follows

$$\eta(\theta) = \frac{1}{N_c} \sum_{i=1}^{N_c} \frac{1}{N_c(i, \theta)} \sum_{j=1}^{N_c(i, \theta)} I_i N_j, \quad (6)$$

where N_c is the total number of cells in the field, I_i is the X-ray flux in C_i , and N_j is the number of galaxies in C_j . The first sum runs over all cells in the field. The second sum runs over all $N_c(i, \theta)$ cells C_j a distance θ away from C_i .

This estimate is slightly different from the more standard one (see e.g. Carrera et al. 1995a,b) which consists in directly averaging $I_i N_j$ over all pairs of cells (C_i, C_j) separated by an angle θ . These two definitions agree in the limit of an infinite field size. For a field of finite size, our definition provides a consistent treatment of boundary cells. For the scrambled data set, the “standard” definition yielded small but significant correlation at large angle, where the finite field effect is most significant. These spurious correlations were absent when we used the definition of equation (6). We also note that, even though the roles of I_i and N_j are not formally symmetric in equation (6), an inversion of N and I did not noticeably affect our measurements.

Both the X-ray and the galaxy data were subject to field-to-field variations due to differences in particle background contamination, solar X-ray contamination, plate sensitivity, seeing, etc. As a result, the fields could not be treated as a single data set. Since, in fact, we intend to focus on angular separations much smaller than the field size ($\theta \ll 1^\circ$), we have instead computed W_{xg} for each field separately. As we will see in §4.1, the distribution of W_{xg} is not gaussian. However, by the central limit theorem, the distribution of the average of W_{xg} over all fields is close to gaussian. A detailed description of the statistics of W_{xg} is given in appendix C. Our final values and 1σ error estimates were thus be taken be

$$W_{xg} \pm \delta W_{xg} \equiv \frac{1}{N_f} \sum_{f=1}^{N_f} W_{xg,f} \pm \frac{1}{\sqrt{N_f}} \sigma_{rms}(W_{xg}), \quad (7)$$

where $W_{xg,f}$ is the value of W_{xg} for the f 'th field, and σ_{rms} is the r.m.s. standard deviation computed over all fields. For the scrambled data set, we constructed $N_{scramble} = 400$ and 200 field pairs for the zero and non-zero lag measurements, respectively. This large number reduces the uncertainty in the mean and in the r.m.s. standard deviation. The final error estimate for the scrambled data set was normalized to N_f .

4. Results

4.1. Zero-Lag Results

As we will see below, most of the correlation signal lies at $\theta = 0$. We therefore first consider the zero-lag results in great detail in order to assess the reality and uncertainty of the signal.

Table 1 gives our measured values of $W_{xg}(\alpha_p, 0)$ in each field for the real data set. Figure 2 shows the distribution of $W_{xg}(\alpha_p, 0)$ in histogram form for the real data set. For comparison, a subset of the scrambled data set containing N_f fields is also shown. There is a small but significant positive offset in the real values which yield a correlation of $W_{xg}(\alpha_p, 0) = .045 \pm .013$, with a

significance of 3.5σ . As noted above, the distribution of W_{xg} is clearly non-gaussian for the real data set. This is not surprising since η (Eq. [3]) is the product of two random variables and is thus expected to follow a skewed distribution. The origin of unusually high correlations for several outlier fields will be discussed in detail in §4.4. Here, we simply note that, after the removal of the six fields with $W_{xg} > .17$, the mean correlation is $W_{xg}(\alpha_p, 0) = .020 \pm .008$, which is now significant at the 2.4σ level. The scrambled set yields a correlation of $W_{xg} = -.001 \pm .008$ which, as expected, is consistent with zero.

Figure 3 shows $W_{xg}(\alpha_{cell}, 0)$ with cell sizes ranging from α_p to $8\alpha_p$ for each of the five data sets. The mean values and their associated errors are listed in table 2. Although the measurements at different cell sizes are not independent, their comparison gives a measure of the robustness of the signal. The real data set yields a positive correlation for all values of α shown. The solar-contaminated and Soft-Galaxies data sets yield lower correlations. As we noted above, this is expected since the large contribution of solar and Galactic X-rays, in each case respectively, results in a smaller relative contribution of the XRB to the observed intensity.

We do not detect any significant correlation between stars and the hard-band XRB. This is somewhat surprising since the contribution of stars to the XRB in ROSAT deep surveys is about 15% (Hasinger 1996), and since stars outnumber galaxies by a factor of about five in our magnitude range. The absence of correlation could be due to the soft nature of characteristic stellar spectra which mitigate their contribution in the hard band. We leave a quantitative discussion of the limits our analysis can place on mean stellar X-ray fluxes and on their contribution to the XRB to future work. The importance of this result in the context of our study of galaxies and the XRB is that it simplifies the interpretation of W_{xg} . We can indeed safely assume that misclassified stars contaminating our galaxy sample do not contribute to the correlation signal.

As expected, the scrambled data set yields correlation values consistent with zero for all α 's. It is worth noting that the uncertainty for the scrambled set ($\delta W_{xg}(\alpha_p, 0) \simeq .008$) represents about 38% of the variance (i.e. the square of the standard deviation) for the real set ($\delta W_{xg}(\alpha_p, 0) \simeq .013$). In general, two effects contribute to the variance of W_{xg} : the intrinsic variation in the correlation signal from one region of the sky to another, and the statistical uncertainty involved in measuring W_{xg} in finite fields. If we take the variance for the scrambled set to be representative of the latter effect, we conclude that the intrinsic field-to-field variation represents about 62% of the variance of W_{xg} . One must therefore be cautious when using bootstrap error estimates since these do *not* account for the intrinsic variance.

As a further test of the reality of the signal, we plotted W_{xg} versus various related parameters in figure 4. No obvious correlations exists between W_{xg} , the mean number of galaxies, the mean XRB flux, Galactic latitude, or the X-ray exposure time. This indicates that our signal does not suffer from major systematic biases.

4.2. Non-Zero-Lag Results

Now that we have established the existence of a significant signal at zero-lag, we can obtain the full correlation information by studying W_{xg} at nonzero-lag. Figure 5 shows our measurement of $W_{xg}(\alpha_p, \theta)$ as a function of θ . The results are shown both for the real and the scrambled data sets. The mean values of W_{xg} and their error bars are listed in table 3 for each value of θ .

As noted above, most of the signal in the real data set lies at small angles ($\theta < 3'$). The scrambled set yields correlations consistent with zero, as expected. The striking feature in figure 5 is the presence of a significant plateau for $\theta \gtrsim 4'$ with an amplitude of $W_{xg}(\alpha_p, \theta \gtrsim 4') \simeq .015$. We will discuss its nature in §4.4.

In figure 6, we plotted the values of W_{xg} at $\theta = 10\alpha_p$ against that at $11\alpha_p$ for each field. A correlation (of the correlation function!) is clearly present. This shows that our measurements of W_{xg} at different values of θ are not statistically independent. This is due to the fact that the PSF (and perhaps the clustering scale) extends beyond one pixel. This correlation must be taken into account when estimating errors or when fitting to the angular dependence of W_{xg} . In appendix C we present a treatment of this correlation using multi-variate gaussian statistics. In particular, we show how one can estimate the covariance matrix $V_{i,j}$ of $W_{xg}(\alpha_p, \theta_i)$ from our data. The resulting values for the elements of $V_{i,j}$, shown in figure 13, demonstrate that the correlation effect is most severe for $\theta \lesssim 3\alpha_p$ and for $\theta \gtrsim 8\alpha_p$.

4.3. Comparison of Zero-Lag and Non-Zero Lag Results

We now consider a comparison of the zero and non-zero lag signals. This is not only a check of the consistency of our results but also allows us to verify the reality of the correlation at large angle which should contribute to the zero-lag correlation for large cell sizes.

For this comparison, we choose a phenomenological form for the underlying correlation function w_{xg} which reproduces the nonzero-lag results and check that it is consistent with the zero-lag results. We take $w_{xg}(\theta)$ to be the sum of a gaussian and a constant, i.e.

$$w_{xg}(\theta) = a_0 + a_1 e^{-\frac{1}{2}(\theta/\theta_0)^2}, \quad (8)$$

where a_0 , a_1 and θ_0 are constants. The estimator W_{xg} can then be computed by introducing equation (8) in equation (5). We obtain

$$W_{xg}(\alpha, \theta) = a_0 + a_1 \Lambda(\alpha, \theta_0, \theta) \quad (9)$$

where Λ is the integral defined in equation (B1). A semi-analytical expression for Λ is given in appendix B.1 and its angular dependence is plotted in figure 12 for $\alpha = \alpha_p$ and $\theta_0 = 0'.5$.

Our best fit parameters for $W_{xg}(\alpha_p, \theta)$ at nonzero-lag are $a_0 = .013$ and $a_1 = .087$. For convenience, we fixed $\theta_0 \equiv \sigma_{psf} = 0'.5$. The result of the fit is shown in figure 5 as the dot-dashed

curve. The resulting cell size dependence of W_{xg} at zero-lag is shown in figure 3, as a similar curve. The agreement is acceptable even though the measured values of W_{xg} are slightly higher than the one inferred from the non-zero lag results. This is probably due to the ambiguity in the treatment of boundary cells (see discussion in §3.2). (In fact, a variation of the pixel inclusion threshold can slightly improve the agreement). Note also that the zero-lag measurements confirms the presence of a significant correlation all the way up to $\alpha \simeq 8'$, which corresponds to $\theta \simeq 4'$.

4.4. Correlation at Large Angles

The plateau in W_{xg} at large angle is rather surprising. Its reality is confirmed both by the scrambled results and by the fact that it appears consistently both in the zero and non-zero lag measurements (at least for $\theta \simeq 4'$).

In previous studies (Lahav et al. 1993; see also the other cross-correlation studies discussed in §1), the correlation signal was taken to arise from two terms in the correlation function: the “Poisson” term and the “clustering” term. The Poisson term corresponds to the case of the galaxies themselves emitting X-rays, and the clustering term corresponds to the spatial clustering of galaxies with discrete X-ray sources. As we will see in detail in §5, these two terms produce, in our context, correlation signals with specific angular dependence given by the two functions Λ and Ξ displayed in figure 12. For both terms, W_{xg} falls off for $\theta \gtrsim 4'$ and thus can not produce the plateau observed in our measurement. This can be seen more quantitatively in figure 5 where the dotted curve correspond to the best fit to the Poisson + clustering terms (see §5.3). The fit is poor for $\theta \gtrsim 4'$.

One possibility is that the plateau is due to the hot X-ray gas in clusters of galaxies. Diffuse emission from the clusters in our fields is mostly, but not completely, removed by our point source excision algorithm and can thus contribute signal to the very sensitive CCF. An example is provided by the field displayed in figure 7. This field has the highest zero-lag value of W_{xg} in our data set (i.e. it is the right-most field in figure 2). A cluster of galaxies appears as an excess in residual X-rays and in the surface density of galaxies in the upper left-hand corner of the field. Bright nearby clusters have typical X-ray sizes of about $10'$, a scale which is consistent with the scale of the plateau. Note that the field displayed in figure 7 is extreme; most fields in our data set, including those with cluster targets, such as the one in figure 1, do not show any obvious cluster emission. A search of the NED database (Helou et al. 1991), indeed reveals that only three of the cluster-target fields have an X-ray detected cluster within a radius of $20'$ of the field center.

To test this hypothesis we use the fact that 29 out of our 62 fields had clusters of galaxies as their *Einstein* targets. These are flagged with a target type of 3 in table 1. (Fields with superclusters as targets often contain clusters of galaxies and were thus also included). In figure 8, we show the value of W_{xg} at $\theta = 0$ vs. that at $\theta = 7\alpha_p$ with different symbols for fields with cluster and with non-cluster targets. The value of $W_{xg}(\alpha_p, 7\alpha_p)$ is taken to be representative of

the plateau for each field and is listed in table 1. As can be seen in this figure, the zero-lag value has little relation to the presence of a cluster, except for a few outliers. This is in contrast with the non-zero lag values which are significantly larger for cluster target fields. The values of W_{xg} as a function of θ for each of the cluster and non-cluster data sets are listed in table 3. At zero-lag, the non-cluster fields yield a mean correlation of $W_{xg}(\alpha_p, 0) = .029 \pm .013$, a significance of 2.2σ . In figure 9, the mean W_{xg} is shown separately for cluster and non-cluster fields. The value for all fields combined is redisplayed for comparison. In spite of the somewhat degraded statistics, it is clear that the plateau is virtually absent for non-cluster target fields, whereas it is enhanced for cluster target fields. This suggests that the plateau is indeed caused by the residual diffuse X-ray emission in clusters of galaxies.

5. Interpretation of the Correlation Function

Now that we have established the existence of a positive correlation signal for our data set, we need to interpret its angular dependence and thus infer information about galaxies and the XRB. For this purpose, Treyer & Lahav (1995) have developed a detailed formalism which involves a projection of the 3-dimensional CCF into 2-dimensions. Here, we consider a similar but fully 2-dimensional approach. This has the advantage of being simple and of involving few model parameters. In addition, we include the effect of the PSF of the X-ray imaging detector. The formalism presented in §5.1 is general and can be adapted to any measurement of the CCF between an imaged diffuse background and a population of discrete sources. After applying this formalism to our specific case in §5.2, we compare its prediction with our non-zero lag measurements in §5.3

5.1. Formalism

In general, the total X-ray flux $I_j \equiv I_j^x$ measured in a cell C_j can be decomposed into

$$I_j^x = I_j^i + I_j^p + I_j^d, \quad (10)$$

where the terms, correspond to the instrumental background (i) (due to cosmic ray interactions, calibration source leakage, and solar-scattered X-rays), the emission from point X-ray sources (p), and the diffuse component of the XRB (d), from left to right respectively. A source is considered discrete if its solid angle is negligible compared to the PSF and to the cell size. Thus, in our situation, the diffuse component of the XRB includes the emission from the intracluster gas in nearby clusters of galaxies. We can also decompose the galaxy catalog object counts $N_j \equiv N_j^o$ in C_j as

$$N_j^o = N_j^g + N_j^s \quad (11)$$

where N_j^g is the number of galaxies (g) in C_j and N_j^s is the number of spurious objects (s) misclassified as galaxies.

Introducing equations (10) and (11) in equation (3), we obtain

$$\eta = \eta_{is} + \eta_{ps} + \eta_{ds} + \eta_{ig} + \eta_{pg} + \eta_{dg} \quad (12)$$

where $\eta_{ab}(\theta) \equiv \langle I_i^a N_j^b \rangle_{\theta_{ij}=\theta}$. As before, the brackets refer to an average over cells separated by an angle θ .

Since the galaxy catalog and the X-ray maps were constructed independently, I^i and N^o are not correlated. Thus, $\eta_{is} + \eta_{ig} = \langle I^i \rangle \langle N^s \rangle + \langle I^i \rangle \langle N^g \rangle$.

As we noted in §4.1, stars are not significantly correlated with the XRB intensity, at least in our experimental conditions. Other misclassified objects such as plate flaws are obviously not correlated with the XRB. We thus obtain $\eta_{ps} + \eta_{ds} = \langle I^p \rangle \langle N^s \rangle + \langle I^d \rangle \langle N^s \rangle$.

We have seen in §4.4 that the diffuse component of the XRB is likely to affect the CCF. An analysis of the diffuse term would involve a modelling of clusters of galaxies and of their redshift distribution. This is beyond the scope of the present study. We therefore leave η_{dg} unexpanded. In §5.3, we will show how we can nevertheless proceed using the subset our measurements for non-cluster target fields.

We are left with $\eta_{pg}(\theta)$ to evaluate. For this purpose, we define the PSF, ψ , so that a point source with flux S_p , placed at $\boldsymbol{\theta}_p$, produces an observed X-ray intensity at $\boldsymbol{\theta}_o$ given by

$$i(\boldsymbol{\theta}_o) = S_p \psi(\boldsymbol{\theta}_{op}). \quad (13)$$

We assume that $\psi(\boldsymbol{\theta})$ is azimuthally symmetric so that it only depends on $\theta \equiv |\boldsymbol{\theta}|$. This definition implies that ψ is normalized so that

$$\int_S d\Omega_s \psi(\theta_s) = 1, \quad (14)$$

where the integral is over the whole sky.

The derivation of η_{pg} using this definition of ψ is given in detail in appendix A. The result consists of the two standard terms (see eg. Treyer & Lahav, 1995) modified to include the effect of the PSF: the ‘‘Poisson’’ term (Eq. [A5]) and the ‘‘clustering’’ term (eq. [A10]). Introducing these results into equations (12) and (2), we finally obtain

$$W_{xg} = W_{xg}^{\text{poisson}} + W_{xg}^{\text{clustering}} + W_{xg}^{\text{diffuse}}, \quad (15)$$

where

$$W_{xg}^{\text{poisson}}(\theta_{12}) = \frac{\langle I^g \rangle}{\langle I \rangle \langle N \rangle} \frac{1}{2\pi\alpha^2} \int_0^{2\pi} d\phi_{12} \int_{C_1} d\Omega'_1 \int_{C_2} d\Omega'_2 \psi(\theta'_{12}) \quad (16)$$

and

$$W_{xg}^{\text{clustering}}(\theta_{12}) = \frac{\langle I^p \rangle \langle N^g \rangle}{\langle I \rangle \langle N \rangle} \frac{1}{2\pi\alpha^4} \int_0^{2\pi} d\phi_{12} \int_{C_1} d\Omega'_1 \int_{C_2} d\Omega'_2 \int_S d\Omega'_s \bar{w}_{pg}(\theta'_{1s}) \psi(\theta'_{2s}). \quad (17)$$

In the two equations above, the $d\Omega'_1$ and $d\Omega'_2$ integrals are over two cells C_1 and C_2 separated by $\boldsymbol{\theta}_{12}$. The $d\Omega'_s$ integral is over the whole sky (S). The brackets denote an average over all available

cells. The function $\overline{w}_{pg}(\theta)$ is the effective CCF between the positions of point X-ray sources and galaxies. It is defined in equation (A9) as the X-ray flux-weighted average of the flux-dependent CCF w_{pg} . That such an averaging is necessary is not surprising since, after all, the X-ray point sources with fluxes just below the excision threshold dominate the anisotropy of the observed XRB and are thus the one most susceptible to producing a correlation with the galaxies. As noted above, the term $W_{xg}^{\text{diffuse}} \equiv (\eta_{dg} - \langle I^d \rangle \langle N^g \rangle) / (\langle I \rangle \langle N \rangle)$ is left unexpanded.

As can be inferred from inspecting their functional form, the three terms above correspond to three distinct effects responsible for a correlation between the XRB and galaxies:

1. Poisson: the galaxies emit X-rays.
2. Clustering: the galaxies are spatially clustered with discrete X-ray sources.
3. Diffuse: the galaxies are spatially clustered with diffuse X-ray emission.

5.2. Application

We can now apply the above formalism to our specific case. For the *Einstein*-IPC, the PSF is gaussian so that, after normalization (Eq. [14]),

$$\psi(\theta) \equiv \frac{1}{2\pi\sigma_{psf}^2} e^{-\frac{1}{2}(\theta/\sigma_{psf})^2} \quad (18)$$

To proceed, we need to know the angular dependence of \overline{w}_{pg} which describes the clustering of galaxies with point X-ray sources. Information about the clustering of sources can be deduced from the measurement of their Auto-Correlation Function (ACF). The angular ACF w_{gg} of galaxies in the southern APM catalog is well described by a power law of the form $w_{gg}(\theta) = (\theta/\theta_{gg})^{-\beta_{gg}}$ in the range $.01^\circ < \theta < 1^\circ$ (Maddox et al. 1990a). The slope was measured to be $\beta_{gg} = .668$ and is magnitude-independent. On the other hand, the correlation amplitude θ_{gg} does depend on magnitude and ranges from about $10''$ to $151''$ for $B_J \simeq 20$ and 17.5 , respectively. Such a scaling of the ACF with magnitude is expected from the projection the spatial ACF into 2-dimensions (Groth & Peebles, 1997; Phillips et al. 1978). Vikhlinin & Forman (1995) studied the clustering of ROSAT X-ray sources with a .5-2 keV flux lower limit of about 10^{-14} ergs cm^{-2} s^{-1} , close to our flux excision limit S_{exc} . They found that the ACF of ROSAT point X-ray sources, w_{pp} , also follows a power law with a slope of $\beta_{pp} = .7 \pm .3$ and a normalization of $\theta_{pp} = 4''$ for θ between $30''$ and $1000''$.

The two slopes β_{gg} and β_{pp} are both consistent with the value $\beta \simeq .7$. It is thus reasonable to assume that the magnitude-dependent CCF, w_{pg} , defined in equation (A7) is also described by a power law of the form: $w_{pg}(S^p, S^g; \theta) = (\theta/\theta_{pg}(S^p, S^g))^{-\beta}$, where S^p and S^g are the X-ray and optical fluxes of the point X-ray sources and galaxies, respectively, and $\beta \simeq .7$. Since the flux

dependence of w_{pg} is limited to its normalization $\theta_{pg}(S^p, S^g)$, we can factor the θ dependence of \bar{w}_{pg} out of the integrals in equation (A9) and obtain

$$\bar{w}_{pg}(\theta) = \left(\frac{\theta}{\bar{\theta}_{pg}} \right)^{-\beta}, \quad (19)$$

where $\bar{\theta}_{pg}$ is left as a free parameter to be determined.

With the specific functional forms of equations (18) and (19), equation (16) becomes

$$W_{xg}^{\text{poisson}}(\alpha, \theta) = \frac{\langle I^g \rangle}{\langle I \rangle \langle N \rangle} \frac{\alpha^2}{2\pi\sigma_{psf}^2} \Lambda(\alpha, \sigma_{psf}, \theta), \quad (20)$$

while equation (17) becomes

$$W_{xg}^{\text{clustering}}(\alpha, \theta) = \frac{\langle I^p \rangle \langle N^g \rangle}{\langle I \rangle \langle N \rangle} \left(\frac{\alpha}{\bar{\theta}_{pg}} \right)^{-\beta} \Xi(\alpha, \sigma_{psf}, \beta, \theta), \quad (21)$$

where Λ and Ξ are the integrals defined in equations (B1) and (B8), respectively. In Appendix B we describe our semi-analytic evaluation of Λ and our numerical evaluation of Ξ . The functions are both displayed in figure 12. Two useful analytical fits to Λ and Ξ for the parameters relevant to the present study are given in equations (B7) and (B9), and are also displayed on this figure. (The analytical fit for Λ is indistinguishable from Λ itself on the figure.)

5.3. Fit Results

Our remaining task is to compare our theoretical expectations with our measurement of the CCF. The three terms contributing to W_{xg} have different angular dependences and can thus, at least in principle, be isolated by a fitting to measurements of W_{xg} at different values of θ .

As we noted in §4.4, the Poisson and clustering terms can not produce the plateau observed for the combined cluster plus non-cluster data set. The best fit parameters to a combination of the poisson term and the clustering term (see Eq. [22] below) are $a_{\text{poisson}} = 0$ and $a_{\text{clustering}} \simeq .05$. (The two parameters are constrained to be positive). The best fit is shown in figure 5 as the dotted curve. As we already noted, the fit is poor for $\theta \gtrsim 4'$.

Given the disappearance of the plateau when only non-cluster target fields are considered (see §4.4), it is likely that the plateau is due to residual diffuse X-ray emission from clusters of galaxies which contribute to W_{xg} through the diffuse term. Although we do not pursue this here, it would be worthwhile to model such diffuse emission and to derive the expected angular dependence of W_{xg}^{diffuse} .

Let us now focus on the non-cluster target fields for which the plateau is virtually absent. If we *assume that the diffuse term is negligible for the non-cluster data set*, we are left to fit

$W_{xg}(\alpha, \theta)$ to the following function

$$W_{xg}(\alpha, \theta) = a_{\text{poisson}}\Lambda(\alpha, \sigma_{psf}, \theta) + a_{\text{clustering}}\Xi(\alpha, \sigma_{psf}, \beta, \theta), \quad (22)$$

where a_{poisson} , and $a_{\text{clustering}}$ are free parameters. So as to reduce the number of free parameters, we fix $\beta = .7$ in accordance with the discussion in §5.2.

We have noticed in §4.2, that the measurements of W_{xg} at different values of θ are not statistically independent. In appendix C, we describe our procedure for the fit (Eq. [C5]) assuming that the set of values of W_{xg} follow a multi-variate gaussian distribution (Eq. [C1]). The covariance matrix (Eq. [C2]) is estimated from the data (Eq. [C4]) and is displayed in figure 13.

The result of the fit to our measurement of $W_{xg}(\alpha_p, \theta)$ for $0 \leq \theta \leq 8\alpha_p$ are displayed in figure 10. This figure shows the constant probability contours of χ^2 (Eq. [C7]) with $9 - 2 = 7$ degrees of freedom. We have used the analytical fits for Λ and Ξ given in equations (B7) and (B9), respectively. The best fit (Eq. [C8]) occurs for $a_{\text{poisson}} = .04 \pm .02$ and $a_{\text{clustering}} = .005 \pm .004$. The errors correspond to the 1σ estimates for each parameter taken separately (Eq. [C10]) and are also displayed on figure 10. The resulting best fit is displayed as the solid line in figure 9.

The value of χ^2 for the best-fit parameters is 5.1. The fit is thus acceptable. It worth noting that a fit which does *not* takes the covariance of W_{xg} into account (i.e. one for which the covariance matrix \mathbf{V} , in Eq. [C2], is diagonal) yields $\chi^2 \simeq 2.1$ which correspond to a fit which is “too good”. The covariance of W_{xg} must therefore be taken into account in order not to underestimate the measurement errors.

By comparing equations (20) and (21) with equation (22), we can deduce the following physical quantities

$$\langle I^g \rangle = \frac{2\pi\sigma_{psf}^2}{\alpha^2} \langle N \rangle \langle I \rangle a_{\text{poisson}} \quad (23)$$

and

$$\bar{\theta}_{pg} = \alpha \left(\frac{\langle I \rangle \langle N \rangle}{\langle I^p \rangle \langle N^g \rangle} \right)^{\frac{1}{\beta}} a_{\text{clustering}}^{\frac{1}{\beta}}. \quad (24)$$

Our measurements for the non-cluster data set yield $\langle N \rangle = .149 \pm .002$ objects per cell and $\langle I \rangle = (3.11 \pm .01) \times 10^{-4}$ cts s^{-1} per cell. From our estimates in section 2, we have $\langle N^g \rangle / \langle N \rangle = .8 \pm .2$ and $\langle I^{XRB} \rangle / \langle I \rangle = .6 \pm .1$. If we assume that the diffuse component of the XRB is negligible, we can set $\langle I^p \rangle \simeq \langle I^{XRB} \rangle$. (Alternatively, any difference between $\langle I^p \rangle$ and $\langle I^{XRB} \rangle$ can be absorbed in the definition of $\bar{\theta}_{pg}$). With these numerical values and setting $\alpha = \alpha_p$, we obtain $\langle i^g \rangle = (2.2 \pm 1.1) \times 10^{-6}$ cts s^{-1} arcmin $^{-2}$ and $\bar{\theta}_{pg} = .10 \pm .16$ arcsec. The errors correspond to 1σ . The implication of these final values are discussed in the next section.

6. Galaxies and the X-Ray Background

6.1. Clustering

Let us first consider our measurement for the galaxy/X-ray-sources clustering amplitude $\bar{\theta}_{pg}$. Our value for $\bar{\theta}_{pg}$ is consistent with 0 at the 1σ level. Note that negative values of $\bar{\theta}_{pg}$ are of course unphysical and are thus excluded. Therefore, we do not detect any significant clustering between discrete X-ray sources and galaxies. Our value for $\bar{\theta}_{pg}$ can thus be interpreted as an upper limit.

As we noted in section 5.2, the amplitudes for the auto-correlation of galaxies (Maddox et al. 1990a) and of ROSAT X-ray sources (Vikhlinin & Forman 1995) are $10'' < \theta_{gg} < 151''$ (for $20.5 > b_J > 17.5$), and $\theta_{pp} \simeq 4''$, respectively. Our value $\bar{\theta}_{pg} = .10 \pm .16$ arcsec is thus considerably smaller than these two amplitudes. In our analysis, we are in effect cross-correlating two population of sources with different mean X-ray flux: the X-ray sources dominated by the sources just below the excision flux limit S_{exc} (i.e. mostly AGN at $z > .2$), and the galaxies (at $z \lesssim .2$), which, as will see below, have a much smaller mean X-ray flux. Thus, it is not surprising that our cross-correlation clustering amplitude be smaller than the two associated auto-correlation clustering amplitudes.

6.2. X-ray Emission from Galaxies

The statistical significance of our detection for the Poisson term is also low: our measurement of $\langle i^g \rangle$ is only 2σ away from 0. This can easily be improved by performing the analysis with a larger number of fields. We can nevertheless draw several useful conclusions from our measurement.

Using our estimation of $\langle I^{XRB} \rangle$ (see section 2), we deduce that the fraction of the XRB contributed by APM galaxies with $13.5 < E < 19$ is $\langle I^g \rangle / \langle I^{XRB} \rangle = .015 \pm .008$ in the hard (.81-3.5 keV) band. This fraction should not be mistaken for the total contribution of APM-like galaxies distributed over all space.

The mean X-ray flux of the catalogued galaxies is easily computed to be $\langle S^g \rangle \equiv \langle i^g \rangle / \langle n^g \rangle = (2.1 \pm 1.1) \times 10^{-5}$ cts s^{-1} in the hard band. The X-ray spectra of galaxies can be described by a thermal bremsstrahlung model with $kT \sim 1 - 2$ keV and $kT \gtrsim 5$ keV, for ellipticals and spirals, respectively (Kim et al. 1992). If we adopt such a model with $kT = 3 \pm 2$ keV and $N_H \simeq 3 \times 10^{20}$ cm^{-2} , the above flux corresponds to $\langle S^g(.81 - 3.5keV) \rangle = (8.1 \pm 4.7) \times 10^{-16}$ ergs cm^{-2} s^{-1} . In the more conventional *Einstein* and ROSAT bands, this corresponds to $\langle S^g(.2 - 4.0keV) \rangle = (9.1 \pm 5.0) \times 10^{-16}$ and $\langle S^g(.5 - 2.0keV) \rangle = (5.4 \pm 3.0) \times 10^{-16}$ ergs cm^{-2} s^{-1} , respectively. We note that this flux is three orders of magnitude below the flux limit of the *Einstein* Medium Sensitivity survey ($\sim 10^{-13}$ ergs s^{-1} cm^{-2} in the .2-4 keV band; see Gioia et al. 1990) and more than one order of magnitude below those for deep ROSAT surveys with mostly complete optical identifications ($\sim 10^{-14}$ ergs s^{-1} cm^{-2} in the .5-2 keV band; see Hasinger 1996). This is of course a consequence of the statistical nature of our measurement.

It is noteworthy that $\langle S^g \rangle$ is about two orders of magnitude below the discrete source

detection threshold in our fields ($\langle S_{exc}(.81 - 3.5\text{keV}) \rangle \simeq 4.8 \times 10^{-14}$ ergs cm $^{-2}$ s $^{-1}$). Even though this seems surprising at first, we will see below that $\langle S^g \rangle$ is consistent with the mean X-ray flux expected for galaxies in our sample, i.e. for galaxies with $\langle E \rangle \simeq 17.5$. On the other hand, galaxies with X-ray fluxes close to S_{exc} are expected to have a mean magnitude of $\langle E \rangle \simeq 13.5$. They are thus, on average, much brighter in the optical than the galaxies we considered. Another way to understand the low value of $\langle S^g \rangle$, is to consider the surface density of X-ray sources. According to the X-ray logN–logS relation measured with ROSAT (Hasinger et al. 1993), the number density of X-ray sources with fluxes above $\langle S_{exc} \rangle$ is $n(> \langle S_{exc} \rangle) \simeq 7$ deg $^{-2}$, much lower than our galaxy surface density ($\langle n^g \rangle \simeq 530$ deg $^{-2}$). On the other hand, an extrapolation of this logN–logS relation yields $n(> \langle S^g \rangle) \sim 10^3$ deg $^{-2}$, close to $\langle n^g \rangle$.

The X-ray emission of “normal” galaxies has been extensively studied in the past (see Fabbiano 1989 for a review). For spiral (S) and irregular (Irr) galaxies, the X-ray emission is dominated by binary X-ray sources and SNR. For elliptical (E) and S0 galaxies, it is likely to be composed of a baseline component of X-ray binaries and a hot gaseous component. Fabbiano et al. (1992) have constructed a catalog of *Einstein* X-ray measurements for more than 450 galaxies. The catalog is mostly optically selected and is thus appropriate for a comparison with our results. We selected the 222 and 132 galaxies with *Einstein*-IPC fluxes classified as “normal” S+Irr and E+S0 galaxies. In figure 11, we show the resulting S(.2-4.0 keV) X-ray fluxes vs. the optical B-magnitudes for S+Irr and for E+S0 galaxies separately. Flux upper limits are indicated by stars. Early-type galaxies tend to have higher X-ray fluxes than late-type galaxies. This is likely due to the contribution of the hot gaseous component which is absent in most late-type galaxies.

For S+Irr galaxies, a correlation between $\log(S)$ and B is significant at the 99.99% confidence level (ignoring upper limits). The correlation for E+S0 galaxies is only significant at the 91% level. These confidence levels were computed using the linear correlation coefficient for detected galaxies. If, as is customary, we assume a constant X-ray-to-optical flux ratio we obtain the relation $\log S = -\frac{2}{5}B - c$, where c is a constant. Ignoring galaxies with upper limits for S, we find $c = -7.9 \pm .6$ and $c = -7.3 \pm .6$, for the late and early type galaxies, respectively. The errors correspond to 1σ . (The above late-type relation is only slightly different from the one proposed by Fabbiano et al. which corresponds to $c = -8 \pm 1$). These relations are shown as the dashed lines in figure 11. Note that the early-type relation must be taken with caution since no strong correlation is found for this sample. In general, the fraction of late-type to early-type galaxies must be known to predict the mean flux of our mixed APM sample. In the absence of a more significant correlation between X-ray and optical flux for the early-type sample, a comparison with each sample separately is sufficient.

Our measurement is shown as the cross in figure 11. The conversion of §2.2 was used to transform $\langle E \rangle$ into $\langle B \rangle = 19.1 \pm .4$. As is apparent on the figure, our results agree within 1σ with the X-ray-to-optical flux relations inferred from the catalog of Fabbiano et al., simultaneously for both the early and late type samples. We conclude that our correlation results are consistent with an extrapolation of the known X-ray-to-optical flux ratio of normal galaxies. Our result therefore

confirm earlier estimates of the contribution of galaxies to the XRB obtained by integrating the optical number-magnitude relation of galaxies combined with the assumed constant X-ray to optical flux ratio. By applying this method to earlier but similar *Einstein* measurements of the X-ray-to-optical flux ratios (Fabbiano & Trinchieri, 1985; Trinchieri & Fabbiano, 1985), Giacconi & Zamorani (1987) concluded that galaxies contribute about 13% of the 2 keV XRB. Our results do not exclude the possibility that a change in the X-ray-to-optical flux ratio for galaxies with $E \gtrsim 19$ results in a larger contribution to the XRB.

7. Conclusions

Our measurement of the cross-correlation function estimator W_{xg} between 62 *Einstein*-IPC fields (.81-3.5 keV) and $13.5 < E < 19$ Northern APM galaxies therefore leads to the following conclusions:

At zero-lag, we detect a 3.5σ correlation signal with an amplitude of $W_{xg}(\alpha_p, 0) = .045 \pm .013$. This signal passes our series of control tests. Intrinsic field-to-field variations contribute about 62% of the variance of W_{xg} . We therefore warn against the sole use of bootstrapping error estimates which do not include this source of uncertainty.

At non-zero lag, the angular dependence of $W_{xg}(\alpha_p, \theta)$ has two main features: the main signal for $\theta \lesssim 4'$ and, for $\theta \gtrsim 4'$, an almost flat plateau with an amplitude of about $W_{xg}(\alpha_p, \theta \gtrsim 5') \simeq .015$. When fields whose *Einstein* targets are cluster of galaxies are removed from our sample, the plateau virtually disappears, and the zero-lag amplitude becomes $W_{xg}(\alpha_p, 0) = .029 \pm .013$. The agreement between zero-lag and non-zero-lag results were shown to be acceptable.

We developed, from first principles, a formalism to interpret the angular dependence of W_{xg} taking into account the PSF of the X-ray imaging detector. We find that the correlation signal can be produced by three distinct effects: 1. the X-ray emission from the galaxies themselves, 2. the clustering of galaxies with discrete X-ray sources, and 3. the clustering of galaxies with diffuse X-ray emission. These three contributions correspond to the Poisson, clustering and diffuse terms in the expansion of W_{xg} . These terms have different angular dependences, and can thus, in principle be isolated with our formalism.

Even though the diffuse component probably contributes little to the total intensity of the XRB, it can have a significant effect on W_{xg} through the diffuse term. It is likely that the diffuse X-ray emission from clusters of galaxies only partially excised by our point-source finding algorithm produces the observed plateau in W_{xg} .

After assuming that the diffuse term is negligible for our non-cluster target subsample and that the CCF between galaxies and X-ray point sources has the form $\overline{w}_{pg}(\theta) = (\theta/\overline{\theta}_{pg})^{-.7}$, we could fit $W_{xg}(\theta)$ with the Poisson+clustering term. For the fit, we took proper care of the statistical correlation of measurements of W_{xg} at different values of θ which were shown not to be statistically

independent. We find that the galaxy X-ray sources correlation amplitude $\bar{\theta}_{pg}$ is $.10 \pm .16$ arcsec. As expected, this is smaller than the amplitude for the autocorrelation of galaxies and X-ray sources separately. Our value for $\bar{\theta}_{pg}$ is consistent with zero at the 1σ level and can thus be taken as an upper limit; we therefore do not detect a significant clustering between galaxies and point X-ray sources.

From the consideration of the fields with non-cluster targets, the mean X-ray intensity produced by galaxies in the .81-3.5 keV band is $\langle i^g \rangle = (2.2 \pm 1.1) \times 10^{-6}$ cts arcmin $^{-2}$ s $^{-1}$ which corresponds to $1.5 \pm .8\%$ of the XRB in this band. The mean X-ray flux of galaxies with $\langle E \rangle = 17.5 \pm .3$ is then $\langle S^g(.81 - 3.5keV) \rangle = (8.1 \pm 4.7) \times 10^{-16}$ ergs s $^{-1}$ cm $^{-2}$. This is well below the flux limits of both *Einstein* and ROSAT surveys with mostly complete optical identifications. A comparison with the X-ray catalog of galaxies of Fabbiano et al. (1992) shows that this flux agrees within 1σ with that expected for both early and late-type galaxies assuming a constant X-ray-to-optical flux ratio. With such an assumption, Giacconi & Zamorani (1987) concluded that normal galaxies contribute about 13% of the 2 keV XRB. Our results, however, do not rule out the possibility of a larger contribution from galaxies with $E \gtrsim 19$.

From an observational standpoint, it would be worthwhile to improve the statistics by increasing the number of fields. It would also be useful to apply the technique with high statistics to deeper galaxy samples and to other X-ray bands. From a theoretical point of view, the diffuse term and, in particular, the effect of diffuse emission from galaxy clusters deserve more attention. Investigations of the non-gaussian distribution of W_{xg} would allow a better treatment of errors and would perhaps allow the extraction of more information from the correlation signal.

It is important to note that our formalism does not require any input parameters. (With better statistics, the exponent for w_{pg} , which was fixed to $\beta = .7$ in this study, can be left as a free parameter). Results for $\langle S^g \rangle$ and $\bar{\theta}_{pg}$ can therefore be considered as measurements rather than as a fit to a model. This cross-correlation technique is thus a powerful way to measure the mean flux and clustering amplitude of sources too faint to be resolved. In addition, if our conclusions regarding the origin of the plateau are confirmed, this technique can perhaps be used to probe faint diffuse X-ray emission which would otherwise be undetectable.

We thank E. Moran for customizing the *Einstein* archive software and S. Maddox and M. Irwin for their help with the APM catalog. We thank O. Lahav, M. Treyer, A. Blanchard, R. Pilla, C. Cress, A. Chen and J. Halpern for useful discussions. We are also grateful to K. Jahoda, the referee, for his detailed comments and suggestions. This research has made use of the NASA/IPAC Extragalactic Database (NED) which is operated by the Jet Propulsion Laboratory, Caltech, under contract with the National Aeronautics and Space Administration. This work was supported by the National Aeronautics and Space Administration under the Long Term Space Astrophysics Research Program grant NAGW2507. This paper is Contribution Number 602 of the Columbia Astrophysics Laboratory.

A. Computation of η_{pg}

In this section we compute η_{pg} , the main ingredient in the interpretation of W_{xg} , taking into account the effect of the PSF of the X-ray instrument. This quantity was defined in Section 5.1 as

$$\eta_{pg}(\theta) \equiv \langle I_i^p N_j^g \rangle_{\theta_{ij}=\theta}, \quad (\text{A1})$$

where I_i^p is the flux in C_i from point X-ray sources, N_j^g is the number of galaxies in C_j , and the average is over cells with separation θ .

Using the definition of the PSF (eq. [13]), we can write

$$I_i^p = \int_{C_i} d\Omega_i \int_S d\Omega_s \hat{i}^p(\boldsymbol{\theta}_s) \psi(\theta_{si}), \quad (\text{A2})$$

where $\hat{i}^p(\boldsymbol{\theta}_s)$ is the intrinsic intensity of the XRB due to point sources at $\boldsymbol{\theta}_s$ (i.e. the intensity which would be measured with a delta-function PSF). The second integral is over the whole sky.

We proceed in the usual way (Treyer & Lahav 1995), by partitioning the sky S and the cell C_j into infinitesimal subcells labeled by k and l , respectively. Then, η_{pg} becomes

$$\eta_{pg} = \left\langle \left(\int_{C_i} d\Omega_i \sum_{k \in S} \delta \hat{I}_k^p \psi(\theta_{ik}) \right) \left(\sum_{l \in C_j} \delta N_l^g \right) \right\rangle \quad (\text{A3})$$

where $\delta \hat{I}_k^p$ is the intrinsic X-ray flux from point sources in subcell k , and δN_l^g is the number of galaxies in the subcell l .

Upon isolating the instances where the k and l subcells coincide, we can separate the above equation into two terms, namely

$$\eta_{pg} = \left\langle \int_{C_i} d\Omega_i \left(\sum_{k \in C_j} \delta \hat{I}_k^p \delta N_k^g + \sum_{k \neq l} \delta \hat{I}_k^p \delta N_l^g \right) \psi(\theta_{ki}) \right\rangle \quad (\text{A4})$$

Following common usage (see eg. Treyer & Lahav, 1995), we denote these two terms by η_{poisson} and $\eta_{\text{clustering}}$, respectively.

A.1. Poisson Term

If the k -subcells are sufficiently small, they will contain either 0 or 1 galaxies. As a result, the quantity inside the bracket in η_{poisson} is equal either to 0 or to the X-ray flux of the galaxy, respectively. Upon replacing the k -summation by an integral, we thus obtain

$$\eta_{\text{poisson}}(\theta_{ij}) = \langle I^g \rangle \frac{1}{2\pi\alpha^2} \int_0^{2\pi} d\phi_{ij} \int_{C_i} d\Omega'_i \int_{C_j} d\Omega'_j \psi(\theta'_{ij}), \quad (\text{A5})$$

where $\langle I^g \rangle$ is the mean X-ray flux emitted by the catalogued galaxies into a cell of side length α . As usual, the $d\phi_{ij}$ integral operates as an azimuthal average over the relative positions of the two cells.

A.2. Clustering Term

The treatment of the clustering term is more complicated. This is due to the fact that this term involves, as its name indicates, the clustering between X-ray sources and galaxies, which, in general, is flux-dependent. Let us thus decompose the product $\delta\hat{I}_k^p\delta N_l^g$ in $\eta_{\text{clustering}}$ (eq. [A4]) as,

$$\langle\delta\hat{I}_k^p\delta N_l^g\rangle=\int dS^p\int dS^g S^p\left\langle\frac{d(\delta N_k^p)}{dS^p}\frac{d(\delta N_l^g)}{dS^g}\right\rangle, \quad (\text{A6})$$

where S^p is the X-ray flux of the X-ray point sources, and S^g is the X-ray (or optical) flux of the galaxies. The quantities $d(\delta N_k^p)/dS^p$ and $d(\delta N_l^g)/dS^g$ are, respectively, the number of X-ray sources and galaxies in the k and l-subcell per unit flux. To simplify the notation, the integration limits relevant for both data sets, although present, have not been displayed explicitly.

For sufficiently small subcells, the product in the bracket is equal to the joint probability $\delta P_{kl}^{pg}(S^p, S^g)$ of finding an X-ray source in the k-subcell with flux S^p and a galaxy in the l-subcell with flux S^g . This probability can be parametrized in terms of the CCF w_{pg} between X-ray sources and galaxies in the usual fashion (see eg. Eq. [1]) as

$$\delta P_{kl}^{pg}(S^p, S^g)=\left\langle\frac{dn^p}{dS^p}\right\rangle\left\langle\frac{dn^g}{dS^g}\right\rangle[1+w_{pg}(S^p, S^g; \theta_{kl})]\delta\Omega_k\delta\Omega_l \quad (\text{A7})$$

where $\delta\Omega_m$ is the solid angle of subcell m , and n refers to the appropriate number of sources per unit solid angle. The flux dependence of w_{pg} is explicitly displayed.

Equation (A6) can thus be conveniently written as

$$\langle\delta\hat{I}_k^p\delta N_l^g\rangle=\langle i^p\rangle\langle n^g\rangle[1+\bar{w}_{pg}(\theta_{kl})]\delta\Omega_k\delta\Omega_l, \quad (\text{A8})$$

where $\langle i^p\rangle=\int dS^p S^p\langle dn^p/dS^p\rangle$ is the mean X-ray intensity due to point sources, and the effective CCF \bar{w}_{pg} is defined by

$$\bar{w}_{pg}(\theta)\equiv\frac{1}{\langle i^p\rangle\langle n^g\rangle}\int dS^p\int dS^g\left\langle\frac{dn^p}{dS^p}\right\rangle\left\langle\frac{dn^g}{dS^g}\right\rangle S^p w_{gp}(S^p, S^g; \theta). \quad (\text{A9})$$

With this in hand, and by turning summations into integrals in the second term of equation (A4), we finally obtain

$$\eta_{\text{clustering}}(\theta_{12})=\langle I^p\rangle\langle N^g\rangle\left[1+\frac{1}{2\pi\alpha^4}\int_0^{2\pi}d\phi_{12}\int_{C_1}d\Omega'_1\int_{C_2}d\Omega'_2\int_Sd\Omega'_s\bar{w}_{pg}(\theta'_{1s})\psi(\theta'_{2s})\right]. \quad (\text{A10})$$

B. Useful Functions

B.1. Semi-analytic Calculation of Λ

In this appendix, we evaluate the integral $\Lambda(\alpha, \sigma, \theta_{12})$. This expression is handy for our phenomenological fit of W_{xg} (§4.3) and appears in the Poisson term of W_{xg} when the effect of

the PSF is taken into account (§5.2). Let us consider two 2-dimensional square cells, C_1 and C_2 , with mutually parallel sides of length α . Denote their separation by the vector $\boldsymbol{\theta}_{12}$ whose polar coordinates are (θ_{12}, ϕ_{12}) in a coordinate system with origin at the center of C_1 . Then, Λ is defined by

$$\Lambda(\alpha, \sigma, \theta_{12}) \equiv \frac{1}{2\pi} \int_0^{2\pi} d\phi_{12} \hat{\Lambda}(\alpha, \sigma, \theta_{12}, \phi_{12}) \quad (\text{B1})$$

where the $d\phi_{12}$ integral operates an azimuthal average of $\hat{\Lambda}$ itself defined by

$$\hat{\Lambda}(\alpha, \sigma, \theta_{12}, \phi_{12}) \equiv \frac{1}{\alpha^4} \int_{C_1} d^2\theta'_1 \int_{C_2} d^2\theta'_2 e^{-\frac{1}{2}(\theta'_{12}/\sigma)^2}, \quad (\text{B2})$$

where the $d^2\theta$ integrals run over the two cells, and $\theta'_{12} = |\boldsymbol{\theta}'_1 - \boldsymbol{\theta}'_2|$. The α^{-4} factor was included to make Λ dimensionless.

In general, the three length scales involved in $\hat{\Lambda}$ (namely α , θ_{12} and σ) are comparable and, thus, one can not apply any simplifying approximations. The integral can nevertheless be performed analytically. For this purpose, let us choose the axes of the above coordinate system to be parallel to the cell sides. One can then conveniently separate $\hat{\Lambda}$ as follows

$$\hat{\Lambda} = \frac{1}{\alpha^4} \tilde{\Lambda}_{12}(\alpha, \sigma, \bar{x}_2) \tilde{\Lambda}_{12}(\alpha, \sigma, \bar{y}_2), \quad (\text{B3})$$

where (\bar{x}_2, \bar{y}_2) are the coordinates of the center of C_2 and,

$$\tilde{\Lambda}(\alpha, \sigma, \bar{t}_2) \equiv \int_{-\alpha/2}^{\alpha/2} dt_1 \int_{\bar{t}_2 - \alpha/2}^{\bar{t}_2 + \alpha/2} dt_2 e^{-\frac{1}{2}(t_2 - t_1)^2/\sigma^2}. \quad (\text{B4})$$

Note that, in this notation, $\bar{x}_2 = \theta_{12} \cos(\phi_{12})$, and $\bar{y}_2 = \theta_{12} \sin(\phi_{12})$. We operate a change of coordinate defined by: $\tau_1 = t_2 - t_1$, $\tau_2 = t_1 + t_2$. The integration region in Eq. B4 turns from a square to a diamond which can be subdivided into four regions. The symmetry about the $\tau_2 = \bar{t}_2$ axis allows integration inside the upper two regions only. Thus, $\tilde{\Lambda}$ becomes

$$\frac{1}{2} \times 2 \left(\int_{\bar{t}_2 - \alpha}^{\bar{t}_2} d\tau_1 \int_{\bar{t}_2}^{\tau_1 + \alpha} d\tau_2 + \int_{\bar{t}_2}^{\bar{t}_2 + \alpha} d\tau_1 \int_{\bar{t}_2}^{-\tau_1 + 2\bar{t}_2 + \alpha} d\tau_2 \right) e^{-\frac{1}{2}(\tau_1/\sigma)^2}. \quad (\text{B5})$$

The $\frac{1}{2}$ factor comes from the Jacobian of the coordinate transformation.

After performing the two integrals in Eq. B5 and after some algebra, we finally get

$$\begin{aligned} \tilde{\Lambda}(\alpha, \sigma, t) &= \sigma^2 \left[e^{-\frac{1}{2}(t+\alpha)^2/\sigma^2} + e^{-\frac{1}{2}(t-\alpha)^2/\sigma^2} - 2e^{-\frac{1}{2}t^2/\sigma^2} \right] \\ &\quad + \sqrt{\frac{\pi}{2}} \sigma \left[-2t \operatorname{erf}\left(\frac{t}{2\sigma}\right) + (t - \alpha) \operatorname{erf}\left(\frac{t - \alpha}{2\sigma}\right) \right. \\ &\quad \left. + (t + \alpha) \operatorname{erf}\left(\frac{t + \alpha}{2\sigma}\right) \right] \end{aligned} \quad (\text{B6})$$

where erf is the error function.

To evaluate Λ we need to average the above result over ϕ_{12} . We do so by numerically averaging $\hat{\Lambda}$ over 20 values of ϕ_{12} between 0 and $\pi/4$. Figure 12 shows the resulting values for $\Lambda(\theta)$ as a function of θ for the parameters relevant to our study, i.e. for $\alpha = \alpha_p = 64''$ and $\sigma = \sigma_{psf} = .5'$. For comparison with other relevant functions, $\Lambda(0)$ was normalized to 1. The actual normalization is $\Lambda(0) \simeq .551$.

It is convenient to fit the following analytical form to $\Lambda(\theta)$

$$\Lambda(\theta) \simeq \lambda_1 e^{-\frac{1}{2}(\theta/\lambda_2)^2}, \quad (\text{B7})$$

where λ_1 and λ_2 are coefficients whose best-fit values are .552 and .677 arcmin, respectively. The fit results in a mean residual RMS of .0052 and is indistinguishable from the solid line in figure 12.

B.2. Numerical Evaluation of Ξ

The other useful function, Ξ , appears in the clustering term of W_{xg} when the effect of the PSF is included (§5.2). Let us consider again the two cells, C_1 and C_2 , described in appendix B.1. The desired function Ξ is defined as

$$\Xi(\alpha, \sigma, \beta, \theta_{12}) \equiv \frac{1}{4\pi^2 \alpha^4 \sigma^2} \int_0^{2\pi} d\phi_{12} \int_{C_1} d\Omega'_1 \int_{C_2} d\Omega'_2 \int_S d\Omega_s \left(\frac{\theta'_{1s}}{\alpha}\right)^{-\beta} e^{-\frac{1}{2}(\theta'_{2s}/\sigma)^2} \quad (\text{B8})$$

where $\theta'_{is} = |\boldsymbol{\theta}'_i - \boldsymbol{\theta}'_s|$, $i = 1, 2$. As usual, the $d\phi_{12}$ integral performs an azimuthal average. The $d\Omega'_1$ $d\Omega'_2$ integrals are over C_1 and C_2 , respectively. The $d\Omega_s$ integral is over the whole sky. The constant in front of the integral was included to make Ξ dimensionless.

Given the cumbersome nature of equation (B8), we approximated Ξ by Monte-Carlo (MC) integration for the parameter values relevant to our analysis, i.e. for $\alpha = \alpha_p = 64''$, $\sigma = \sigma_{psf} = .5'$, and $\beta = .7$. The desired accuracy was set to .04, and the all-sky integral was approximated by a square cell of side $25\alpha_p$ centered on the midpoint between C_1 and C_2 .

The result of the MC integration is shown in figure 12 for values of θ ranging from 0 to $8'$. As before, Ξ has been normalized to 1 at $\theta = 0$. Its actual normalization is $\Xi(0) \simeq 1.480$.

It is here also convenient to fit $\Xi(\theta)$ with an analytical function to facilitate modelling of the observed correlation function. We choose the form

$$\Xi(\theta) \simeq \left(\frac{\sqrt{\theta^2 + \xi_0^2}}{\alpha}\right)^{-\beta} \quad (\text{B9})$$

where ξ_0 is the only free parameter. The best fit occurs for $\xi_0 \simeq .573 \pm .008$ arcmin and yields a reduced χ^2 of .32 for 28 degrees of freedom. The result of the fit is also shown in figure 12. The power law $(\theta/\alpha)^{-\beta}$ (after being renormalized) is also plotted and can be seen to agree well with Ξ for $\theta \gtrsim 3'$. This is to be expected since this power law is the asymptotic form of equation (B8) for $\theta \gg \alpha, \sigma$.

C. Statistics of W_{xg}

In this appendix, we describe our treatment of the statistics of W_{xg} taking into account their non-gaussian nature and the correlation between measurements at different angular lags. We first show how we can approximate the distribution of our data with the multi-variate gaussian distribution (§C.1). We then estimate the covariance of W_{xg} from the data (§C.2). Finally, in §C.3, we apply these results to the fit of our measurement to the Poisson+Clustering model of equation (22). While most of the following treatment is standard, we have used the formalism and notation given in Lupton (1993).

C.1. Multi-Variate Gaussian Approximation

Let us consider the distribution of W_{xg} at a given angular lag θ_i . For simplicity, let $W_{f,i} \equiv W_{xg,f}(\alpha_p, \theta_i)$, where f refers to one of the N_f fields in our data set and $i = 1, \dots, N_\theta$. Let us denote the intrinsic mean and rms standard deviation of the distribution of $W_{f,i}$ as \overline{W}_i and σ_{W_i} , respectively.

One complication comes from the fact that $W_{f,i}$ is, in general, not normally distributed (see figure 2). Nevertheless, by the central limit theorem, the distribution of the average $W_i \equiv \sum_{i=1}^{N_f} W_{f,i}/N_f$ is close to a normal distribution with mean \overline{W}_i and standard deviation $\sigma_{W_i}/\sqrt{N_f}$, if N_f is sufficiently large. In the case of our non-cluster-target data set, N_f is equal to 33 and should be large enough to satisfy this condition.

Another complication comes from the fact that the distribution of the W_i 's at different i 's are, in general, not independent. This can be seen in figure 6. This is due to the fact that the same fields are used for the measurements at each θ_i and that the PSF (and the galaxy/X-ray-sources CCF w_{gp} , if present) extend beyond one pixel. As a result, the joint distribution of the W_i 's can not be assumed to be simply the product of normal distributions.

We choose the simplest approximation to the joint distribution of correlated normal variables, namely the multi-variate normal distribution. Under this approximation, the joint Probability Distribution Function (PDF) for the averages $\mathbf{W} \equiv (W_1, \dots, W_{N_\theta})^T$ is

$$p(\mathbf{W}) = \frac{1}{\sqrt{(2\pi)^{N_\theta} |V|}} \exp(-(\mathbf{W} - \overline{\mathbf{W}})^T \mathbf{V}^{-1} (\mathbf{W} - \overline{\mathbf{W}})/2) \quad (\text{C1})$$

where $\overline{\mathbf{W}} = (\overline{W}_1, \dots, \overline{W}_{N_\theta})^T$, and \mathbf{V} is the $N_\theta \times N_\theta$ covariance matrix which is given by

$$\mathbf{V} = \langle (\mathbf{W} - \overline{\mathbf{W}})(\mathbf{W} - \overline{\mathbf{W}})^T \rangle. \quad (\text{C2})$$

The quantity $|V|$ is the determinant of \mathbf{V} , and the superscript T stands for transpose. An estimate for \mathbf{V} from the data is derived in the next section.

C.2. Estimate for the Covariance

Let us consider a large number N_r of realizations of our experiment. This would involve the measurement of $W_{xg}(\theta_i)$ for $N_r \times N_f$ fields. Our actual measurement is, say, the $r = 1$ realization. Let us denote the resulting measurements as $W_{r,f,i}$, and their average within realization r as $W_{r,i} \equiv \langle W_{r,f,i} \rangle_f$. In the previous expression and hereafter, a bracket of the form $\langle \dots \rangle_l$ denotes an average over the index l .

We can then express equation (C2) as

$$\begin{aligned} V_{i,j} &\simeq \left\langle (W_{r,i} - \overline{W}_i)(W_{r,j} - \overline{W}_j) \right\rangle_r \\ &= \frac{1}{N_f^2} \sum_{f=1}^{N_f} \sum_{f'=1}^{N_f} \langle W_{r,f,i} W_{r,f',j} \rangle_r - \overline{W}_i \overline{W}_j. \end{aligned} \quad (\text{C3})$$

When $f \neq f'$, $W_{r,f,i}$ and $W_{r,f',j}$ correspond to measurements in different fields and are thus independent. Hence, $\sum_{f \neq f'} \langle W_{r,f,i} W_{r,f',j} \rangle_r = N_f(N_f - 1) \overline{W}_i \overline{W}_j$. On the other hand, when $f = f'$, $W_{r,f,i}$ and $W_{r,f,j}$ involve measurements in the same field and are thus *not* independent. To estimate this term from the available data, we approximate $\langle W_{r,f,i} W_{r,f,j} \rangle_r \simeq \langle W_{1,f,i} W_{1,f,j} \rangle_f$, where, as noted above, the $r = 1$ realization corresponds to our actual experiment. Then, $\sum_{f=f'} \langle W_{r,f,i} W_{r,f,j} \rangle_r \simeq \sum_f W_{1,f,i} W_{1,f,j}$.

By combining the $f \neq f'$ and $f = f'$ terms into equation (C3) and after using the approximation $\overline{W}_k \simeq \langle W_{f,k} \rangle_f \equiv W_k$, we finally obtain

$$V_{ij} \simeq \frac{1}{N_f} \langle (W_{f,i} - W_i)(W_{f,j} - W_j) \rangle_f, \quad (\text{C4})$$

where the $r = 1$ subscript has been dropped. Note that the diagonal elements, V_{ii} are simply equal to $\langle (W_{f,i} - W_i)^2 \rangle_f / N_f \simeq \sigma_i^2 / N_f$, as they should be.

Our measurement of the covariance matrix \mathbf{V} for the non-cluster data set is displayed in figure 13. Correlations at low ($\theta \lesssim 3\alpha_p$) and at high ($\theta \gtrsim 8\alpha_p$) angular lags are clearly visible.

C.3. Fit to Linear Model

In §5.3, we need to fit our measurements of \mathbf{W} to the function $\mathbf{f}(\boldsymbol{\theta}; \mathbf{a}) \equiv a_{\text{poisson}} \Lambda(\boldsymbol{\theta}) + a_{\text{clustering}} \Xi(\boldsymbol{\theta})$, where $\mathbf{a} \equiv (a_{\text{poisson}}, a_{\text{clustering}})^T$ (Eq. [22]). This corresponds to a fit to the $N_a = 2$ parameter linear model (see eg. Lupton 1993, p.81)

$$\mathbf{W} = \mathbf{f}(\boldsymbol{\theta}; \mathbf{a}) + \boldsymbol{\epsilon} \equiv \mathbf{M}\mathbf{a} + \boldsymbol{\epsilon}, \quad (\text{C5})$$

where \mathbf{M} is a $N_\theta \times N_a$ matrix with rows equal to $(\Lambda(\theta_i), \Xi(\theta_i))$, $i = 1, \dots, N_\theta$, and $\boldsymbol{\epsilon}$ is the N_θ -dimensional vector of errors with $\langle \boldsymbol{\epsilon} \rangle = \mathbf{0}$ and covariance matrix $\langle \boldsymbol{\epsilon} \boldsymbol{\epsilon}^T \rangle \equiv \mathbf{V}$.

Within the multi-variate approximation of equation (C1), the probability density for our data set \mathbf{W} to result from a model with parameters \mathbf{a} is

$$p(\mathbf{W}; \mathbf{a}) = \frac{1}{\sqrt{(2\pi)^{N_\theta} |V|}} e^{-X^2(\mathbf{W}; \mathbf{a})/2}, \quad (\text{C6})$$

where,

$$X^2(\mathbf{W}; \mathbf{a}) \equiv (\mathbf{W} - \mathbf{f}(\boldsymbol{\theta}; \mathbf{a}))^T \mathbf{V}^{-1} (\mathbf{W} - \mathbf{f}(\boldsymbol{\theta}; \mathbf{a})). \quad (\text{C7})$$

The best fit to our model corresponds to the value $\hat{\mathbf{a}}$ of \mathbf{a} for which $p(\mathbf{W}; \mathbf{a})$ is maximum. Setting the derivative of X^2 to 0 yields

$$\hat{\mathbf{a}} = (\mathbf{M}^T \mathbf{V}^{-1} \mathbf{M})^{-1} \mathbf{M}^T \mathbf{V}^{-1} \mathbf{W}. \quad (\text{C8})$$

Note that $\hat{\mathbf{a}}$ is a bilinear combination of multi-variate normal variables and thus itself follows a multivariate normal distribution (with two variables). Thus, the PDF of $\hat{\mathbf{a}}$ is

$$p(\hat{\mathbf{a}}) = \frac{1}{\sqrt{2\pi|U|}} \exp(-(\hat{\mathbf{a}} - \bar{\mathbf{a}})^T \mathbf{U}^{-1} (\hat{\mathbf{a}} - \bar{\mathbf{a}})/2), \quad (\text{C9})$$

where $\mathbf{U} \equiv \langle (\hat{\mathbf{a}} - \bar{\mathbf{a}})(\hat{\mathbf{a}} - \bar{\mathbf{a}})^T \rangle$ is the covariance matrix of $\hat{\mathbf{a}}$, and $\bar{\mathbf{a}}$ corresponds to the true distribution of \mathbf{W} , i.e. $\bar{\mathbf{W}} = \mathbf{f}(\boldsymbol{\theta}; \bar{\mathbf{a}})$. By combining equations (C8) and (C2), it is easy to show that $\mathbf{U} = (\mathbf{M}^T \mathbf{V}^{-1} \mathbf{M})^{-1}$. Taken individually, each of the a_i 's are normally distributed with standard deviations simply given by

$$\sigma_{\hat{a}_i} = U_{ii}. \quad (\text{C10})$$

These standard deviations are the estimates for the 1σ errors of the best-fit parameters taken separately.

A measure of the goodness of fit is provided by $X^2(\mathbf{W}; \hat{\mathbf{a}})$. This quantity follows a χ^2 -distribution with $N_\theta - N_a$ degrees of freedom. Its value must be close to $N_\theta - N_a$ for the fit to be acceptable.

Figure 10 shows the probability contours for X^2 in the \mathbf{a} -plane for our fit to the non-cluster data set. The best fit parameters (Eq. [C8]) and their associated uncorrelated 1σ errors (Eq. [C10]) are also shown.

REFERENCES

- Barcons, X., Franceschini, A., De Zotti, G., Danese, L., & Miyaji, T., 1995, *ApJ*, 455, 480
 Boyle, B. J., Griffiths, R. E., Shanks, T., Stewart, G. C., & Georgantopoulos, I., 1993, *MNRAS*, 260, 49
 Boyle, B. J., McMahon, R. G., Wilkes, B. J., & Elvis, M., 1995, *MNRAS*, 272, 462

- Butcher, H. R., & Oemler, A. Jr., 1985, *ApJS*, 57, 665
- Butcher, J. A., et al., 1994, *MNRAS*, in press
- Carballo, R., et al., 1995, *MNRAS*, 277, 1312
- Carrera, F. J., Barcons, X., Butcher, J. A., Fabian, A. C., Lahav, O., Stewart, G. C., & Warwick, R. S. 1995a, *AdSpR*, 16, 111
- , 1995b, submitted to *MNRAS*
- De Zotti, G., Toffolatti, L., Franceschini, A., Barcons, X., Danese, L., & Burigana, C. 1995. in *Proc. of the International School of Space Science 1994 course: X-Ray Astronomy.* ed G. Bignami et al. in preparation.
- Fabbiano, G., & Trinchieri, G., 1985, *ApJ*, 296, 430
- Fabbiano, G., 1989, *ARA&A*, 27, 87
- Fabbiano, G., Kim, D.-W., & Trinchieri, G., 1992, *ApJS*, 80, 531
- Fabian, A. C., & Barcons, X. A. 1992, *ARA&A*, 30, 429
- Giacconi, R., et al. 1979, *ApJ*, 230, 540
- Giacconi, R., & Zamorani, G., 1987, *ApJ*, 313, 20
- Gioia, I. M., Maccacaro, R. E., Schild, R. E., Wolter, A., Stocke J. T., Morris, S. L., & Henry, J. P., 1990, *ApJS*, 72, 567
- Groth, E. J., & Peebles, P. J. E., 1977, *ApJ*, 217, 385
- Hamilton, T., Helfand, D. J., & Wu, X., 1991, *ApJ*, 379, 576
- Hasinger, G., 1996, in *Examining the Big Bang and Diffuse Background Radiations*, eds Kafatos, M., & Kondo, Y. (Netherlands: IAU), 245
- Hasinger, G., Burg, R., Giacconi, R., Hartner, G., Schmidt, M., Trumper, J., & Zamorani, G., 1993, *A&A*, 275, 1. Erratum in *A&A*, 291, 348
- Helou, G., Madore, B. F., Schmitz, M., Bicay, M. D., Wu, X., & Bennett, J., 1991, in *Databases and On-Line Data in Astronomy*, eds Egret, D., & Albrecht, M. (Dordrecht: Kluwer)
- Humphreys, R. M., Landau, R., Ghigo, F. D., & Zumach, W., 1991, *ApJ*, 102, 395
- Irwin, M., & McMahon R. G., 1992, *Gemini*, 37,1
- Irwin, M., Maddox, S., & McMahon, R. G., 1994, *Spectrum*, 2, 14
- Jahoda, K., Lahav, O., Mushotzky, R. F., & Boldt, E., 1991, *ApJ*, 378, L37. Erratum in 1992, *ApJ*, 399, L107
- Jones, L. R., et al., 1995, in *Proc. of the 35th Herstmoncioux Conference: Wide-Field Spectroscopy and the Distant Universe*, eds Maddox, S., & Aragon-Salamanca, A. (Singapore: World Scientific Publishing)

- Kibblewhite et al. 1984. Astronomical Microdensitometry Conference, NASA Conf. Pub., 2317, 277
- Kim, D.-W., Fabbiano, G., & Trinchieri, G., 1992, ApJS, 80, 645
- Koo, D. C, & Kron, R. G., 1992, ARA&A, 30,613
- Lahav, O., et al., 1993, Nature, 364, 693
- Lupton, R., 1993, Statistics in Theory and Practice (Princeton: Princeton Univ. Press)
- Maddox, S. J., Efstathiou, G., Sutherland, W. J., & Loveday, J. 1990a. MNRAS, 242, 43p
- Maddox, S. J., Sutherland, W. J., Efstathiou, G., & Loveday, J., 1990b, MNRAS, 243, 692
- Maddox, S. J., Sutherland, W. J., Efstathiou, G., Loveday, J., & Peterson, B. A., 1990c, MNRAS, 247, 1p
- Mather, J. C., et al., 1990, ApJ, 354, L37
- Metcalf, N., Shanks, T., Fong, R., & Jones, L. R., 1991, MNRAS, 249, 498
- Miyaji T., Lahav O., Jahoda K., & Boldt E. 1994, ApJ, 434,424
- Mushotzky, R. & Jahoda, K., 1992, in The X-Ray Background, eds. Barcons, X. & Fabian, A. C. (Cambridge: Cambridge University Press), 80
- Phillips, S., Fong, R., Ellis, R. S., Fall, S. M., & MacGillivray, H. T., 1978, MNRAS, 182, 673
- Peebles, P. J. E., 1980, The Large-Scale Structure of the Universe. (Princeton: Princeton Univ. Press)
- Refregier A., Helfand D. J., & McMahon R. G, 1995, in proceedings of the conference Röntgenstrahlung from the Universe, held in Würzburg, Germany in Sept 95. in press.
- Roche N., Shanks T., Georgantopoulos I., Stewart G. C., Boyle B. J., & Griffiths R. E. 1995, MNRAS, 273, L15
- Romero-Colmenero, E., Branduardi-Raymont, G., Carrera, F. J., Jones, L. R., Mason, K. O., McHardy, I. M., & Mittaz, J. P. D., 1996, preprint, astro-ph/9604134
- Setti, G., & Comastri, A., 1996, in Examining the Big Bang and Diffuse Background Radiations, eds Kafatos, M., & Kondo, Y. (Netherlands: IAU), 263
- Stocke, J. T., et al., 1991, ApJS, 76, 813
- Treyer M. A., & Lahav O. 1995, submitted to MNRAS
- Trinchieri, G., & Fabbiano, G., 1985, ApJ, 296, 447
- Vikhlinin, A., & Forman, W. 1995, ApJ, 455, L109
- Vikhlinin, A., Forman, W., Jones, C., & Murray, S., 1995a, ApJ, 451, 542
- , 1995b, ApJ, 451, 553
- , 1995c, ApJ, 451, 564

Wang, Q., Hamilton, T., Helfand, D. J., & Wu, X., 1991, ApJ, 374, 475

Wu, X., Hamilton, T., Helfand, D. J., & Wang Q. 1991, ApJ, 379, 564

Zamorani, G. 1995. in Background Radiation Meeting (1993). ed Calzetti, D., et al. (Cambridge: Cambridge Univ. Press)

Table 1. Field characteristics and cross-correlation results

Seq. No. ^a	POSS ^b	R.A. ^c	Dec. ^c	b ^d	t_{exp} ^e	Target ^f	$\langle I \rangle^g$	$\langle N \rangle^h$	$W_{xg}(0)$	$W_{xg}(7\alpha_p)$
29	756	17h 09m 59s	71d 09m 59s	33.7	20053	4	2.44	0.194	-0.048	-0.015
270	1201	01h 16m 29s	08d 13m 59s	-53.7	15572	3	2.49	0.072	0.074	-0.001
280	1563	12h 24m 59s	09d 29m 59s	71.2	41941	3	3.67	0.101	0.081	0.019
294	779	23h 48m 23s	26d 52m 59s	-33.8	10722	3	3.15	0.146	-0.004	-0.008
322	1093	16h 15m 47s	35d 04m 59s	45.6	8377	3	3.36	0.146	0.023	0.090
330	1069	17h 00m 59s	33d 50m 59s	36.2	6058	3	3.74	0.268	0.181	0.143
351	887	04h 30m 29s	05d 14m 59s	-27.4	26346	2	2.99	0.101	-0.077	-0.002
352	1367	12h 07m 59s	39d 39m 59s	75.1	6151	2	3.25	0.121	0.154	-0.014
486	456	08h 38m 01s	13d 23m 04s	30.1	11777	2	2.89	0.172	-0.007	0.002
499	1336	07h 40m 56s	38d 00m 30s	26.1	11357	2	2.75	0.188	-0.039	-0.036
543	1130	21h 34m 03s	00d 18m 11s	-35.7	8145	2	3.06	0.238	0.020	0.033
554	661	09h 23m 55s	39d 15m 22s	46.2	7807	2	3.04	0.149	-0.003	-0.051
1759	601	01h 02m 23s	32d 29m 59s	-30.0	9856	3	3.47	0.173	-0.028	0.014
2003	769	17h 26m 59s	50d 11m 59s	33.5	19069	2	3.03	0.118	-0.078	-0.025
2113	1353	11h 10m 59s	22d 23m 59s	67.3	4402	2	2.71	0.108	-0.049	0.047
2598	316	23h 17m 43s	07d 45m 46s	-48.5	8724	3	3.82	0.132	0.078	0.023
3438	743	16h 27m 57s	40d 58m 11s	43.5	6001	3	3.81	0.300	0.111	-0.033
3954	11	03h 12m 30s	14d 17m 55s	-35.7	11405	3	2.45	0.102	-0.089	0.003
4303	1385	12h 13m 11s	13d 22m 59s	73.7	7731	3	3.05	0.106	0.045	0.003
4374	601	00h 55m 05s	30d 04m 58s	-32.5	14281	2	2.62	0.157	0.044	0.051
4496	932	03h 34m 13s	00d 25m 28s	-41.6	1507	1	3.54	0.065	-0.089	0.032
5391	110	12h 57m 44s	35d 53m 59s	81.3	38271	4	2.66	0.137	0.117	-0.038
5392	110	13h 01m 11s	35d 53m 59s	81.1	37802	4	2.80	0.108	-0.028	-0.031
5394	1259	01h 12m 44s	-01d 42m 53s	-63.7	12830	2	2.61	0.083	0.138	0.004
5425	1372	16h 35m 26s	11d 55m 40s	35.0	6379	2	4.06	0.233	0.018	0.052
5504	924	08h 49m 36s	28d 30m 59s	37.7	16489	1	2.85	0.135	-0.028	-0.029
5688	1414	17h 03m 59s	60d 47m 59s	36.4	18837	2	2.96	0.180	0.121	0.011
5721	1560	12h 28m 43s	07d 41m 52s	69.7	25140	4	3.30	0.053	0.213	-0.008
6083	1259	01h 12m 35s	-00d 01m 59s	-62.1	10458	3	3.32	0.125	0.252	0.199
6084	1259	01h 22m 59s	-01d 45m 59s	-63.1	8273	3	3.29	0.126	0.067	0.092
6104	1429	15h 10m 17s	07d 36m 59s	51.2	7729	3	4.25	0.175	0.081	0.195
6366	136	15h 47m 29s	12d 32m 59s	45.8	11061	2	3.62	0.205	0.045	-0.008
6828	1244	00h 38m 13s	32d 53m 41s	-29.7	10833	3	2.72	0.096	-0.005	-0.019
6830	425	03h 03m 30s	17d 07m 06s	-34.8	11762	3	2.40	0.163	-0.019	-0.019
6832	1369	16h 00m 22s	41d 09m 42s	48.7	9377	3	2.86	0.153	0.080	-0.000
6986	1560	12h 19m 21s	04d 45m 05s	66.3	10273	3	3.14	0.071	-0.005	0.004
6994	1576	12h 22m 52s	18d 27m 59s	79.2	10053	3	2.79	0.036	0.407	0.001
7036	1398	12h 15m 35s	28d 27m 10s	82.5	10073	2	2.92	0.153	0.034	0.050
7039	1578	12h 49m 48s	-00d 55m 39s	61.7	12049	2	3.07	0.045	0.200	-0.014
7397	1069	16h 56m 01s	35d 25m 04s	37.5	10257	1	2.96	0.178	-0.008	0.008
7480	83	16h 04m 49s	15d 59m 37s	43.4	5814	2	3.52	0.273	0.070	0.012
7605	799	21h 42m 06s	14d 32m 35s	-28.3	9138	2	2.80	0.141	0.049	0.002
7769	1051	14h 00m 35s	09d 22m 59s	65.3	6646	3	3.32	0.174	0.020	0.032
7858	83	16h 04m 21s	17d 55m 44s	44.2	10538	3	3.82	0.190	0.036	0.063
8366	1225	01h 46m 42s	34d 56m 12s	-26.2	12328	3	2.97	0.352	-0.060	0.025
8468	65	14h 27m 43s	10d 56m 43s	61.6	9014	2	3.03	0.184	-0.032	-0.042
8672	745	17h 12m 59s	64d 39m 59s	34.8	7878	3	3.25	0.290	0.135	0.069
8926	745	17h 10m 59s	63d 39m 59s	35.2	7818	3	3.52	0.280	0.443	0.200
8982	1051	14h 13m 33s	13d 34m 17s	65.9	9832	2	3.60	0.097	0.060	-0.032
9084	11	03h 08m 30s	14d 28m 53s	-36.2	11920	3	3.09	0.113	0.016	0.024
10087	1174	22h 34m 01s	28d 13m 20s	-25.6	6490	2	2.73	0.286	0.087	0.041
10379	1202	02h 13m 46s	17d 52m 40s	-40.3	8817	3	3.25	0.110	-0.026	0.035

Table 1—Continued

Seq. No. ^a	POSS ^b	R.A. ^c	Dec. ^c	b ^d	t_{exp} ^e	Target ^f	$\langle I \rangle$ ^g	$\langle N \rangle$ ^h	$W_{xg}(0)$	$W_{xg}(7\alpha_p)$
10384	1421	14h 44m 03s	07d 41m 21s	56.4	6548	3	3.24	0.133	0.011	-0.015
10393	1440	14h 26m 33s	01d 30m 36s	55.1	2238	2	3.06	0.110	0.088	-0.099
10437	1051	14h 14m 13s	09d 06m 38s	62.8	9294	2	3.78	0.142	0.011	-0.032
10452	1283	02h 35m 06s	01d 45m 29s	-51.2	16227	3	3.28	0.074	-0.043	0.051
10464	1119	15h 32m 46s	23d 40m 05s	53.0	16905	2	3.11	0.131	0.008	-0.017
10474	1087	14h 44m 35s	11d 47m 59s	58.8	9729	3	3.93	0.145	0.053	-0.019
10533	1056	16h 48m 41s	05d 04m 59s	28.9	33324	2	4.39	0.208	-0.005	0.018
10632	363	03h 23m 37s	02d 14m 46s	-42.4	9269	1	4.00	0.121	-0.046	0.033
10671	860	21h 44m 01s	04d 20m 30s	-35.3	10532	3	3.36	0.114	-0.066	0.005
10682	1195	00h 14m 19s	16d 19m 59s	-45.5	16733	0	2.56	0.104	0.018	-0.030

^a*Einstein* Observatory sequence number

^bPOSS E-plate number

^cRight Ascension and Declination (1950)

^dgalactic latitude ($^{\circ}$)

^e*Einstein*-IPC Exposure time for VG=1-2 (s)

^f*Einstein* target type: 1 = galactic sources, 2 = discrete extragalactic sources (galaxies, QSO, etc), 3 = clusters of galaxies and superclusters, 4 = deep surveys; one field, labeled 0, has no target type specified in the *Einstein* database

^gMean X-ray intensity (10^{-4} cts s^{-1} arcmin $^{-2}$)

^hMean galaxy counts (arcmin $^{-2}$)

Table 2. Zero-lag results. The values for $W_{xg}(\alpha, 0)$ are given for the real (hard-galaxies) and control data sets. The cell size α is shown in units of the pixel size $\alpha_p = 64''$, and the errors correspond to 1σ .

α/α_p	hard-gals	hard-gals(sol)	soft-gal	hard-stars	scrambled
1	0.045±0.012	0.029±0.012	0.013±0.011	0.002±0.004	0.004±0.006
2	0.037±0.011	0.030±0.010	0.013±0.010	0.001±0.003	0.003±0.006
3	0.035±0.011	0.026±0.009	0.013±0.009	0.004±0.003	-0.005±0.005
4	0.019±0.008	0.020±0.009	0.015±0.006	0.000±0.002	0.002±0.004
5	0.023±0.009	0.020±0.007	0.020±0.007	0.001±0.002	0.003±0.004
6	0.022±0.008	0.019±0.006	0.004±0.005	0.001±0.002	0.001±0.003
7	0.021±0.007	0.017±0.006	0.008±0.004	-0.001±0.001	0.002±0.003
8	0.020±0.007	0.016±0.007	0.010±0.004	0.001±0.001	0.000±0.002

Table 3. Non-zero lag results. The value for $W_{xg}(\alpha_p, \theta)$ at different values of θ is given for the whole data set (all) and for the subsamples containing only fields with cluster and non-cluster targets. The results for the scrambled set are given in the last column. The angular lag θ is shown in units of the pixel size $\alpha_p = 64''$.

θ/α_p	all	cluster	non-cluster	scrambled
0	0.045±0.013	0.064±0.023	0.029±0.013	-0.002±0.010
1	0.028±0.008	0.041±0.016	0.018±0.007	-0.000±0.005
2	0.018±0.009	0.037±0.016	0.002±0.007	-0.000±0.004
3	0.013±0.007	0.022±0.012	0.005±0.005	0.001±0.003
4	0.021±0.007	0.042±0.013	0.002±0.004	-0.001±0.003
5	0.014±0.007	0.030±0.013	0.000±0.003	0.002±0.003
6	0.014±0.007	0.031±0.013	-0.000±0.005	0.002±0.003
7	0.015±0.006	0.034±0.011	-0.001±0.004	-0.001±0.003
8	0.016±0.005	0.028±0.011	0.005±0.004	0.000±0.003
9	0.014±0.005	0.027±0.010	0.003±0.005	0.001±0.003
10	0.019±0.005	0.030±0.009	0.010±0.006	0.003±0.003
11	0.012±0.006	0.025±0.010	0.000±0.005	0.003±0.004
12	0.014±0.005	0.023±0.008	0.006±0.006	0.004±0.004

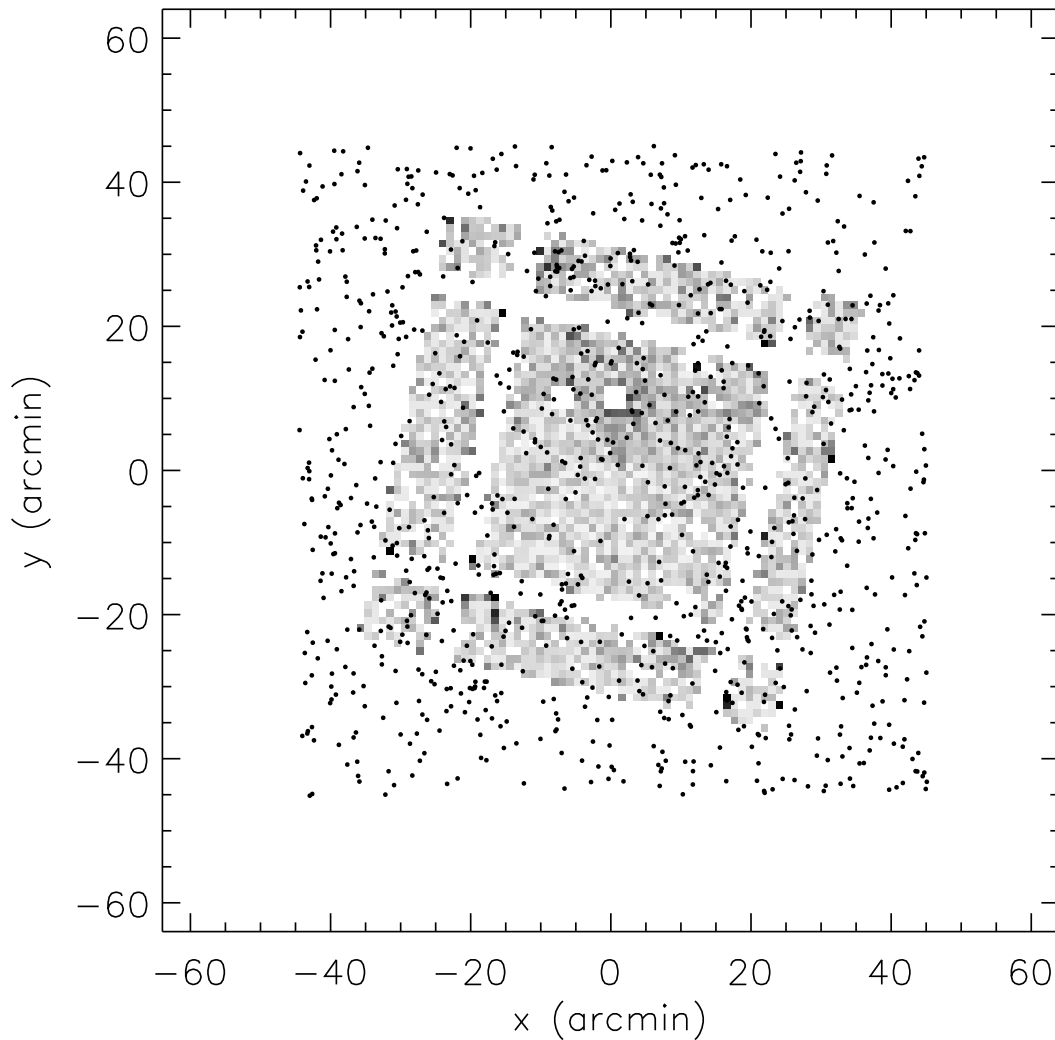


Fig. 1.— Example for a XRB galaxy field pair. This field corresponds to *Einstein*-IPC sequence number 2598. The axes give offsets from the center positions with R.A. and Dec. increasing in the negative-x and positive-y directions, respectively. The .81-3.5 keV XRB intensity is shown as the grey-scale map. Positions of APM galaxies with $13.5 < E < 19.0$ are shown as filled circles.

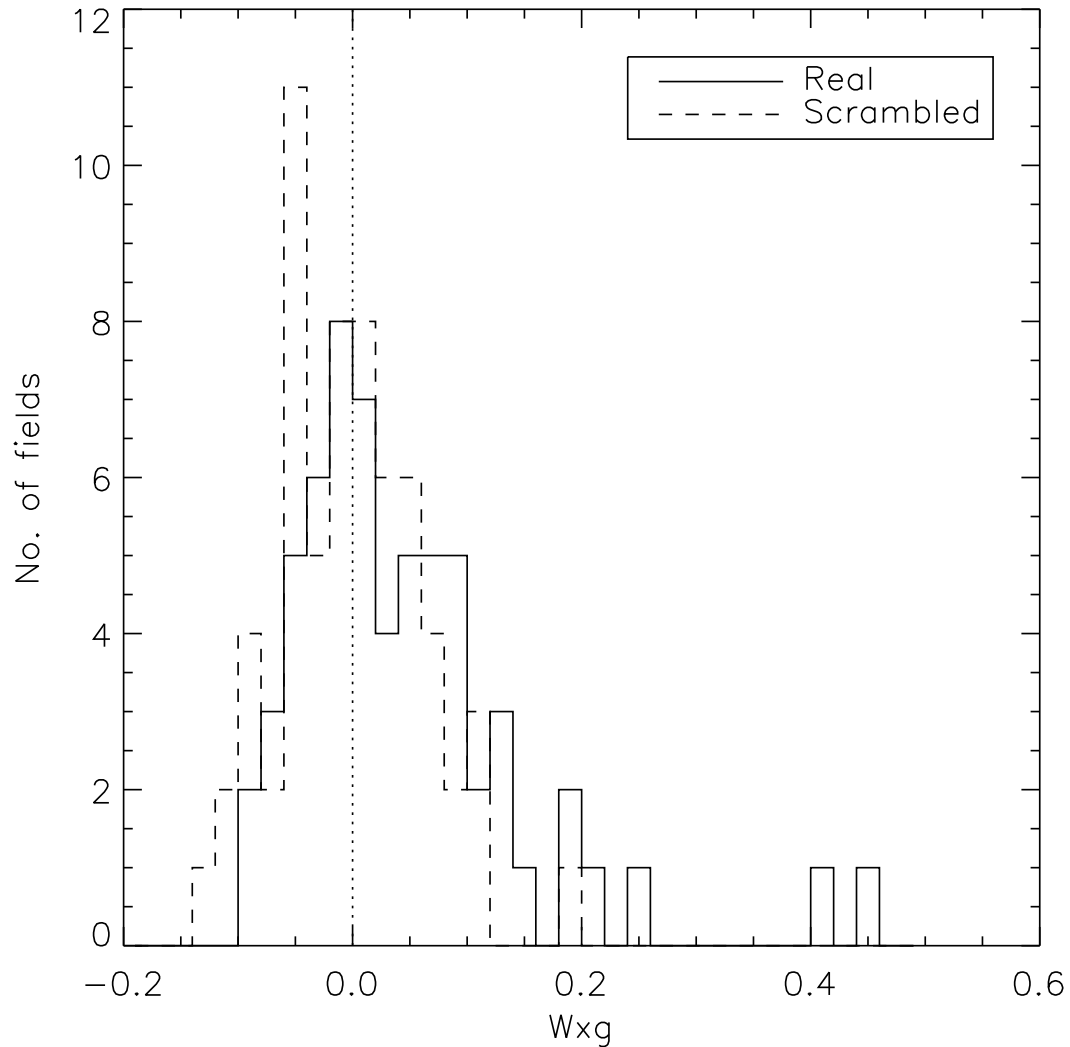


Fig. 2.— Distribution of $W_{xg}(\alpha_p, 0)$ for the real and scrambled data sets. The mean values are $.04 \pm .01$ and $-.001 \pm .008$ for the real and scrambled sets, respectively.

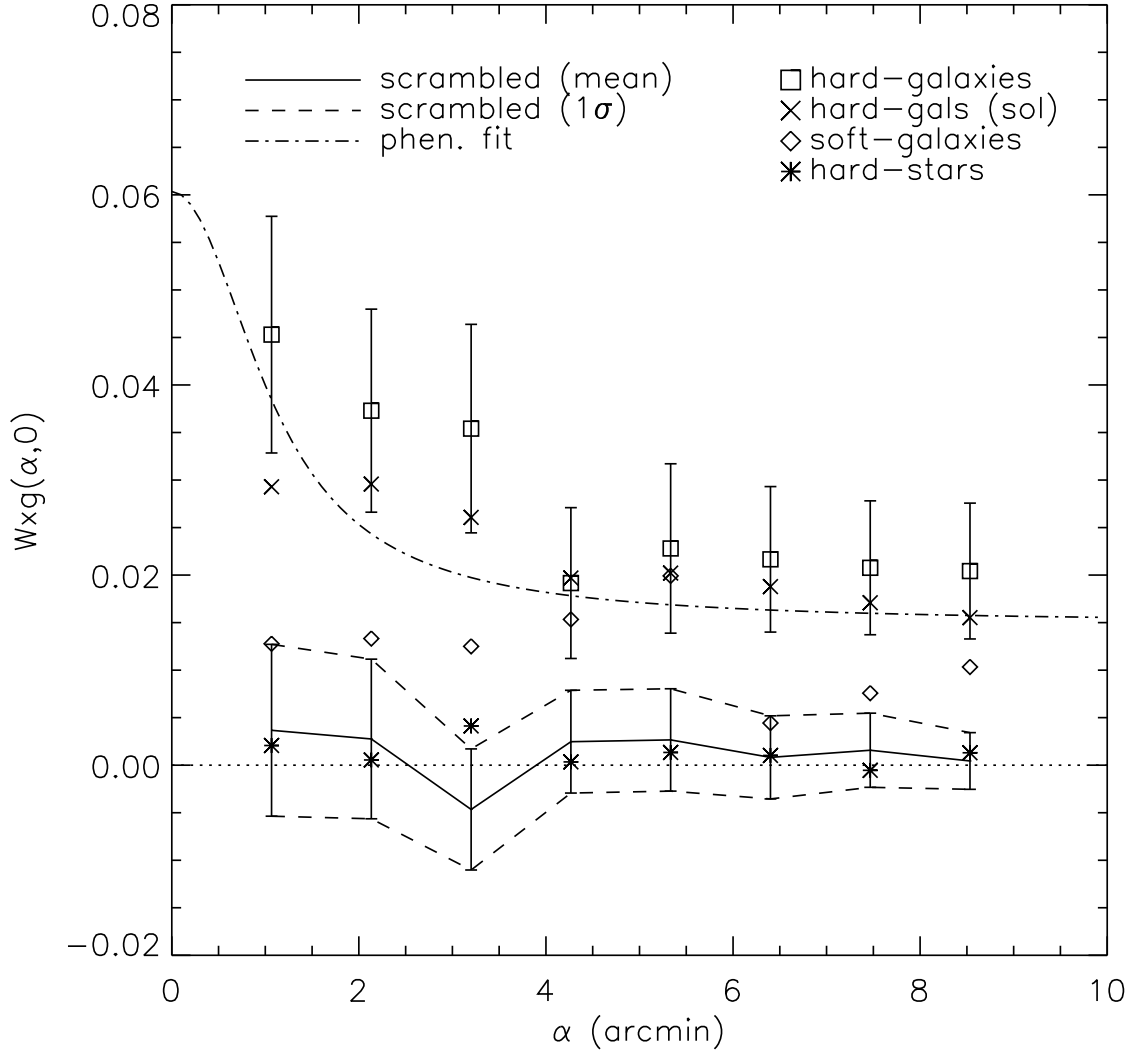


Fig. 3.— Zero-lag results. The values for $W_{xg}(\alpha, 0)$ is shown as a function of cell size α for the real (hard-galaxies) data set and for the control data sets (hard XRB with high solar contamination and galaxies, soft XRB and galaxies, hard XRB and stars, hard XRB with galaxies for scrambled field pairs for which the dashed lines delimit the $\pm 1\sigma$ uncertainties). The dotted-dashed line correspond to the zero-lag values expected from our phenomenological fit to the non-zero-lag results (see text).

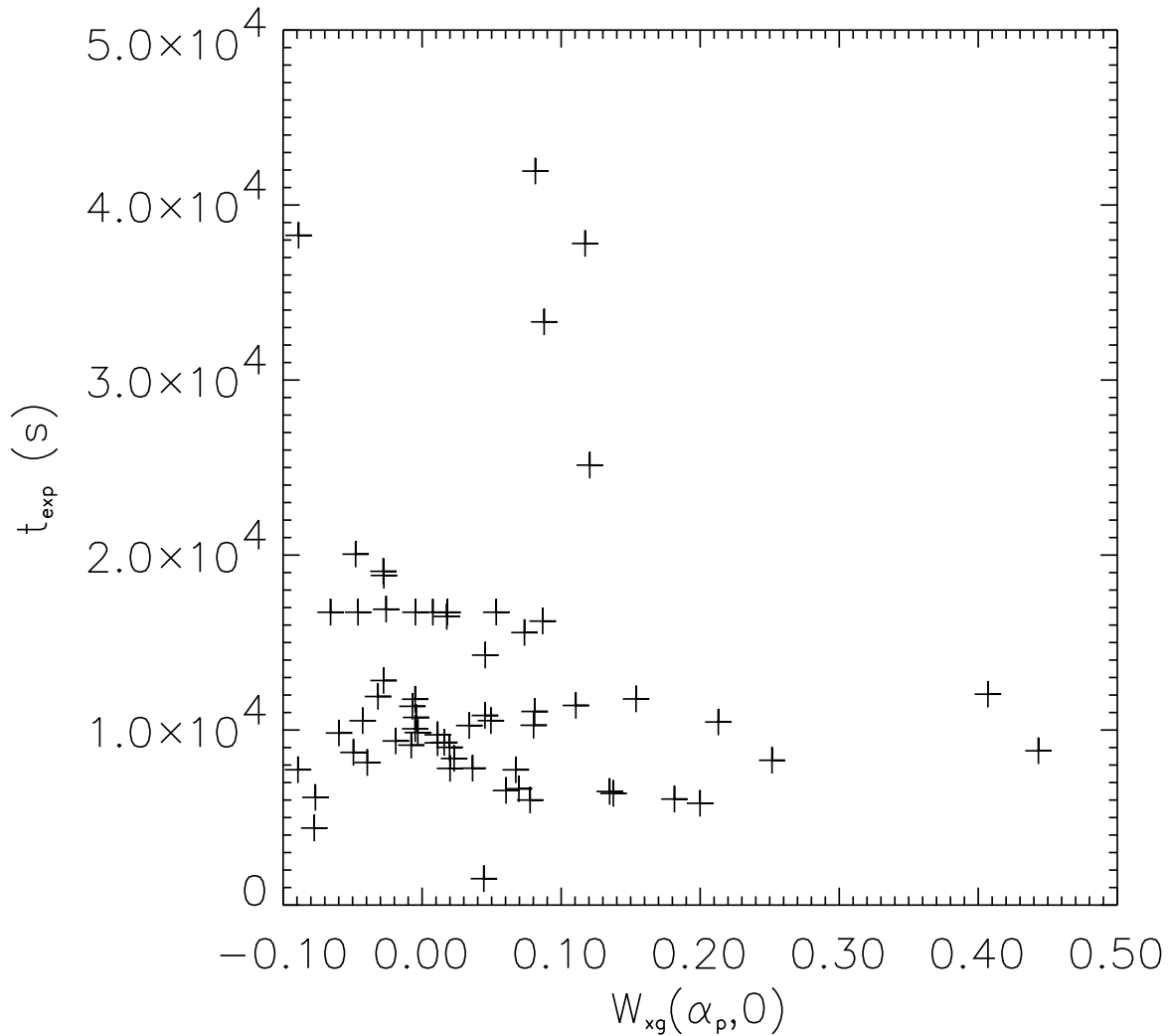


Fig. 4.— $W_{xg}(\alpha_p, 0)$ for the real data set vs. various quantities: (a) *Einstein*-IPC exposure time; (b) absolute Galactic latitude; (c) mean XRB flux in the .81-3.5 keV band (VG=1-2); and (d) mean number of APM galaxies with $13.5 < E < 19$.

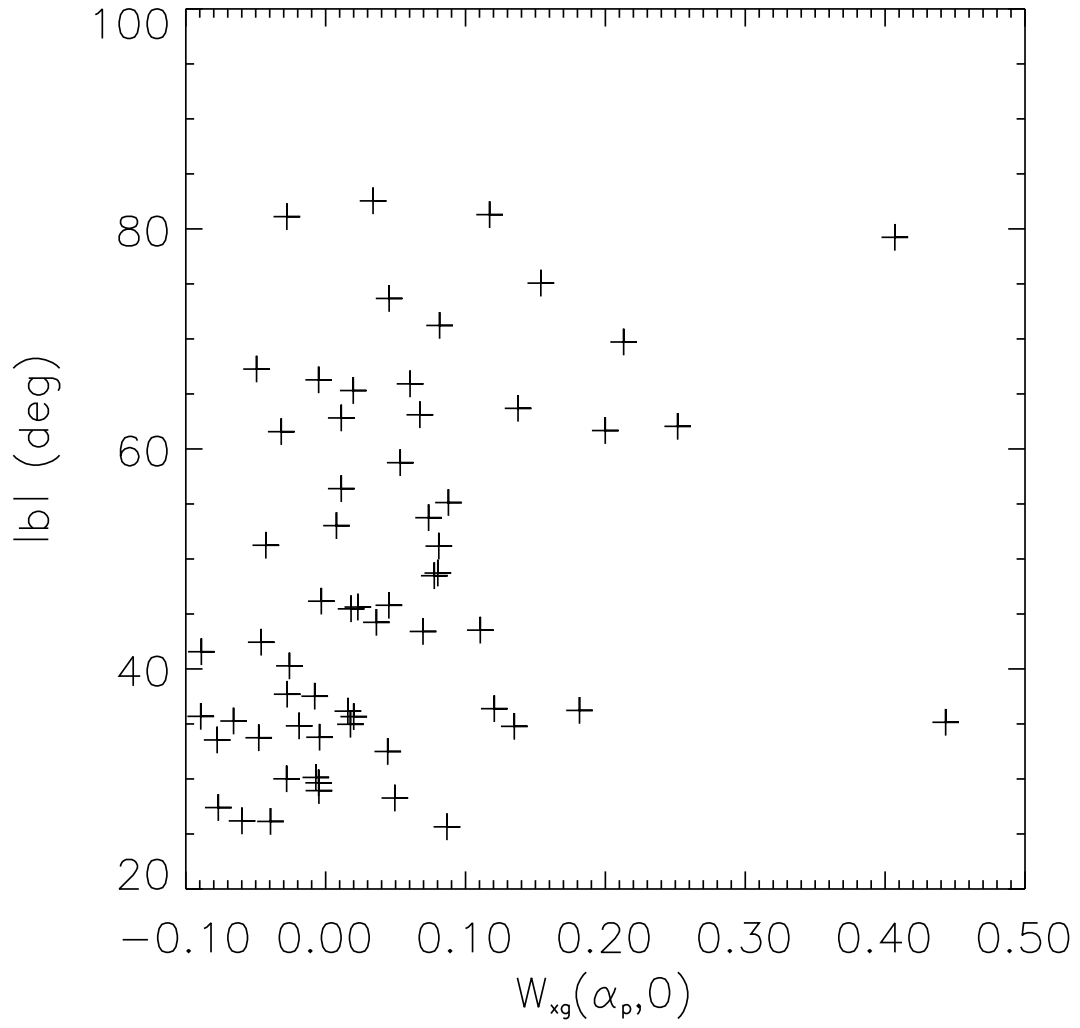


Fig. 4b.—

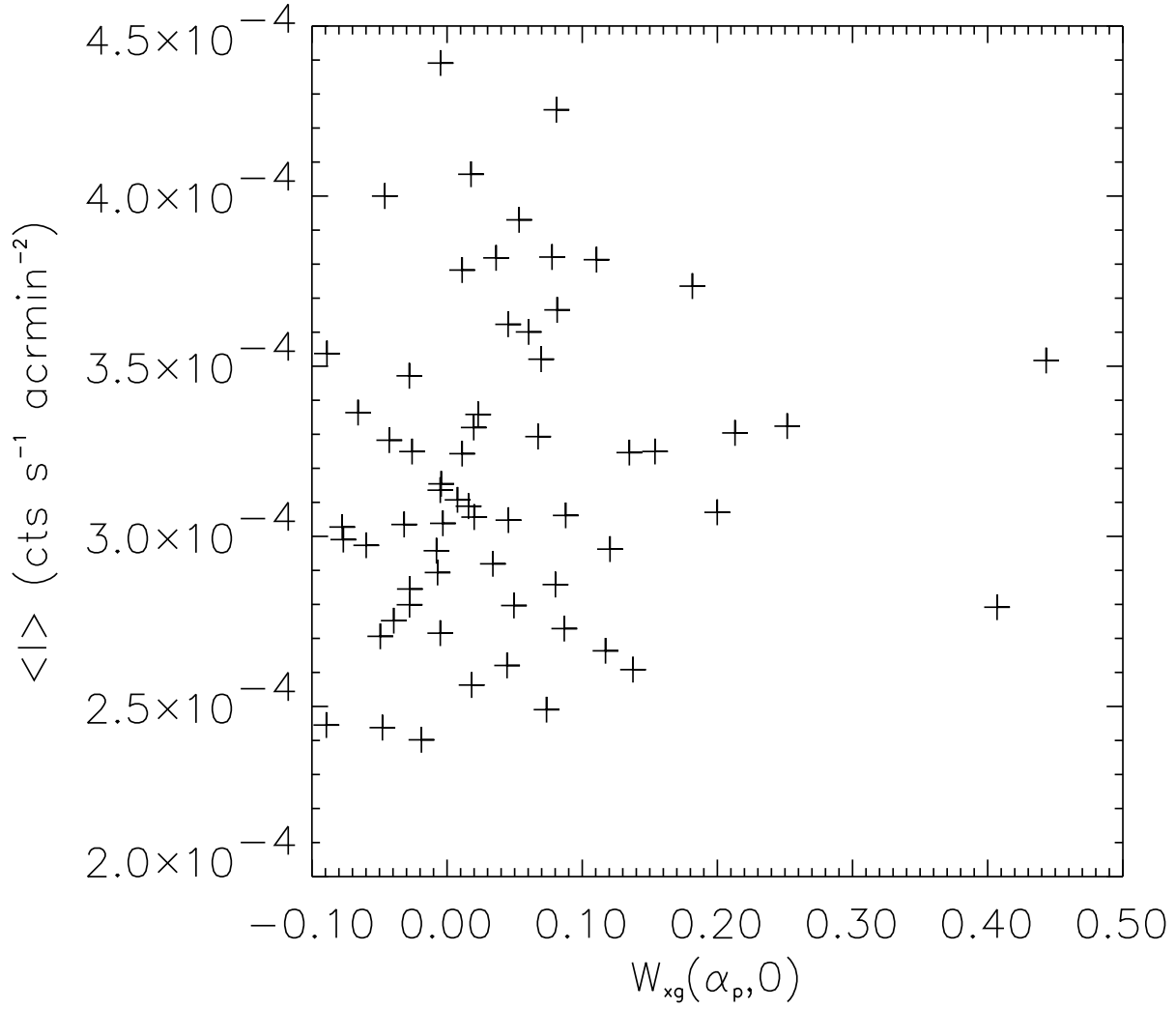


Fig. 4c.—

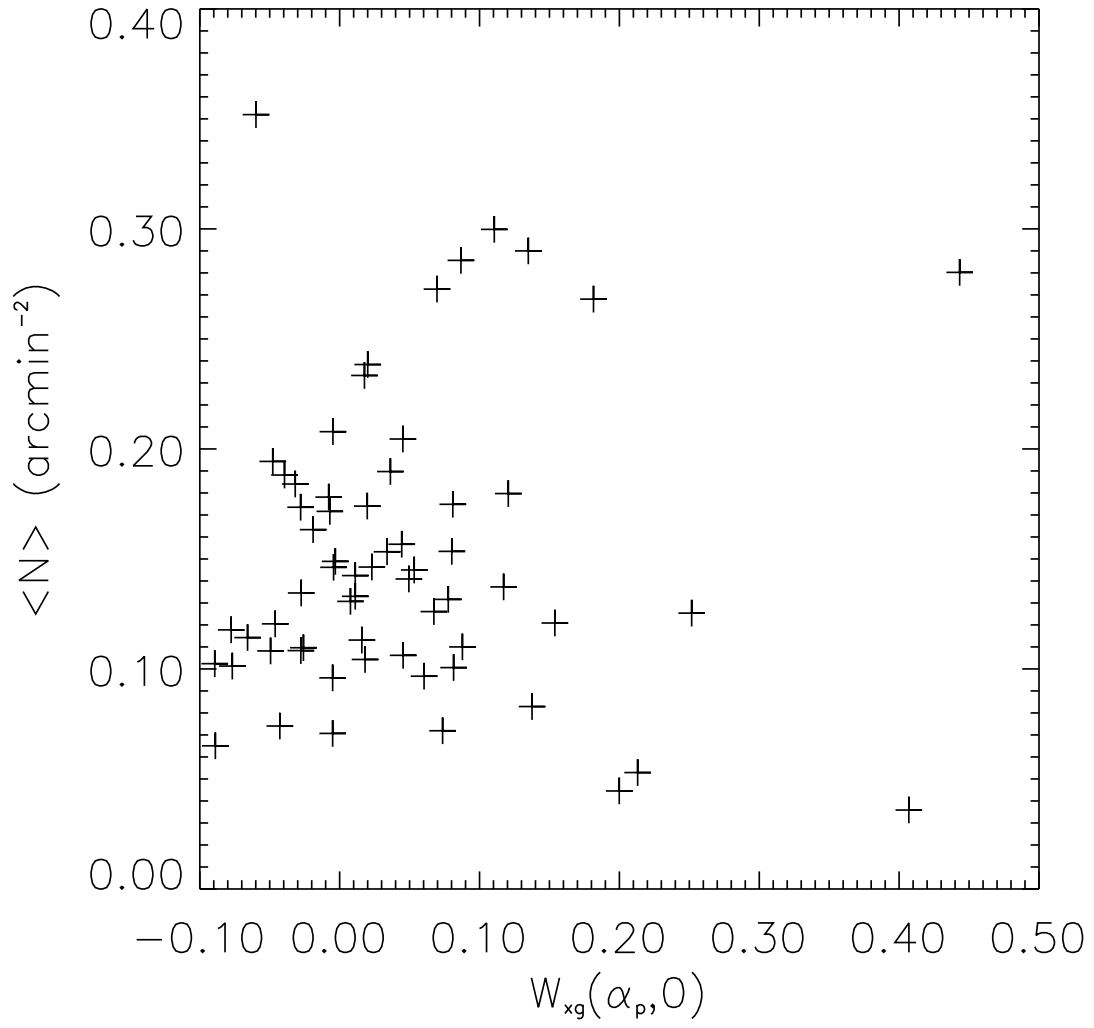


Fig. 4d.—

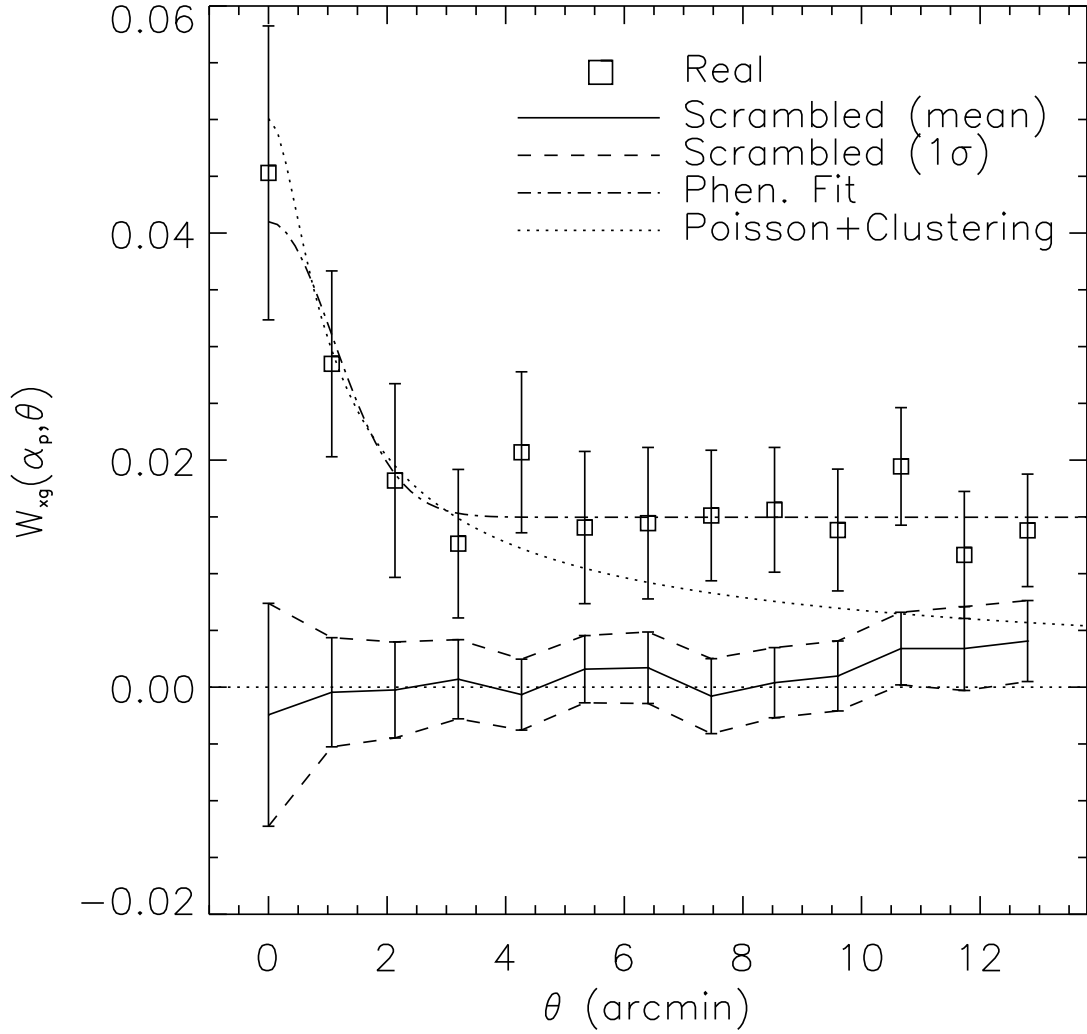


Fig. 5.— Non-zero lag results. $W_{xg}(\alpha_p, \theta)$ vs. θ for the real and the scrambled data set. The dot-dashed curve shows the result of a phenomenological fit used for a comparison with the zero-lag results. The dotted curve corresponds to the best fit to the Poisson + clustering terms, while constraining the fit parameters to be positive.

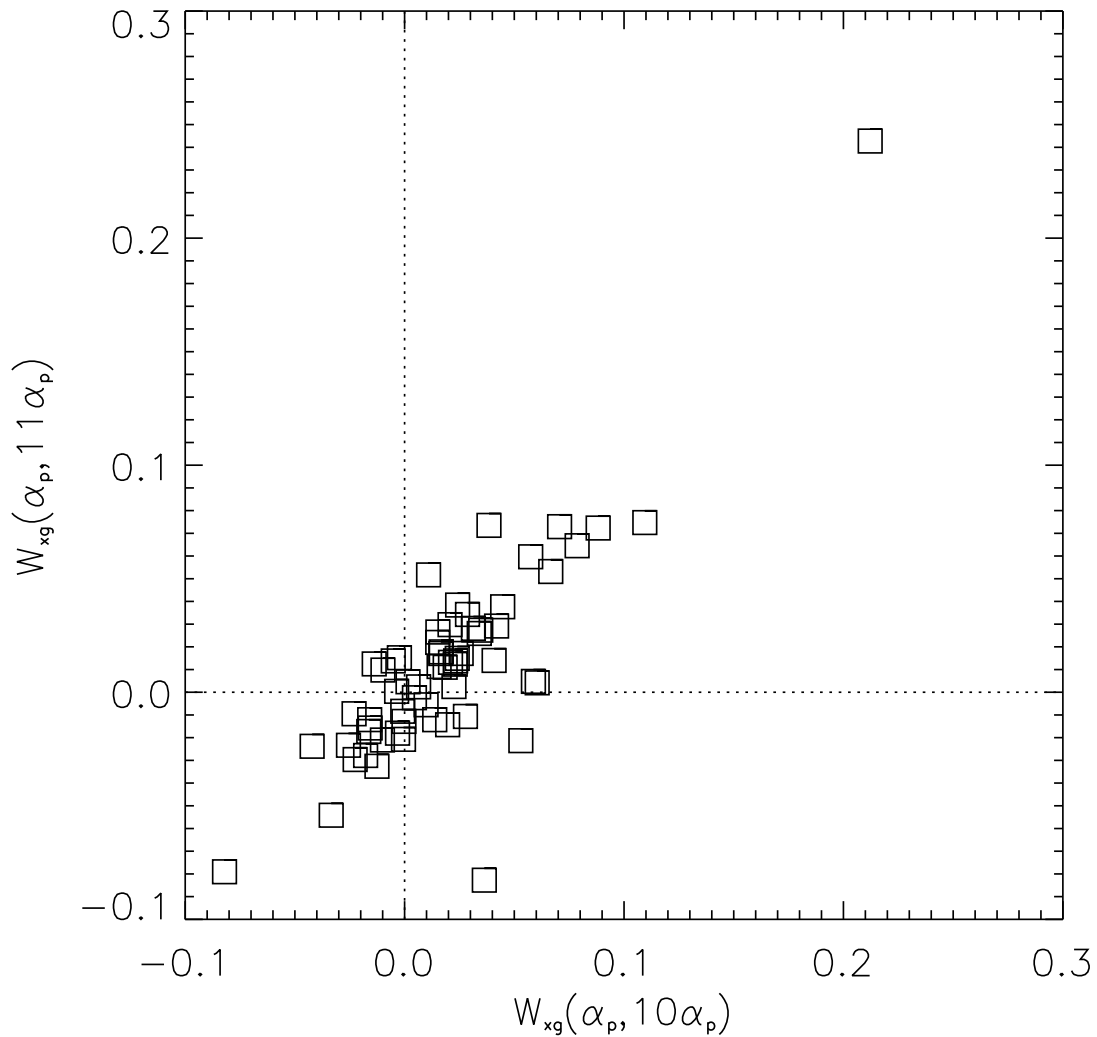


Fig. 6.— Illustration of the correlation between measurements of $W_{xg}(\alpha_p, \theta)$ at different values of θ . For each of the 62 fields, W_{xg} at $\theta = 10\alpha_p$ is plotted against that at $\theta = 11\alpha_p$.

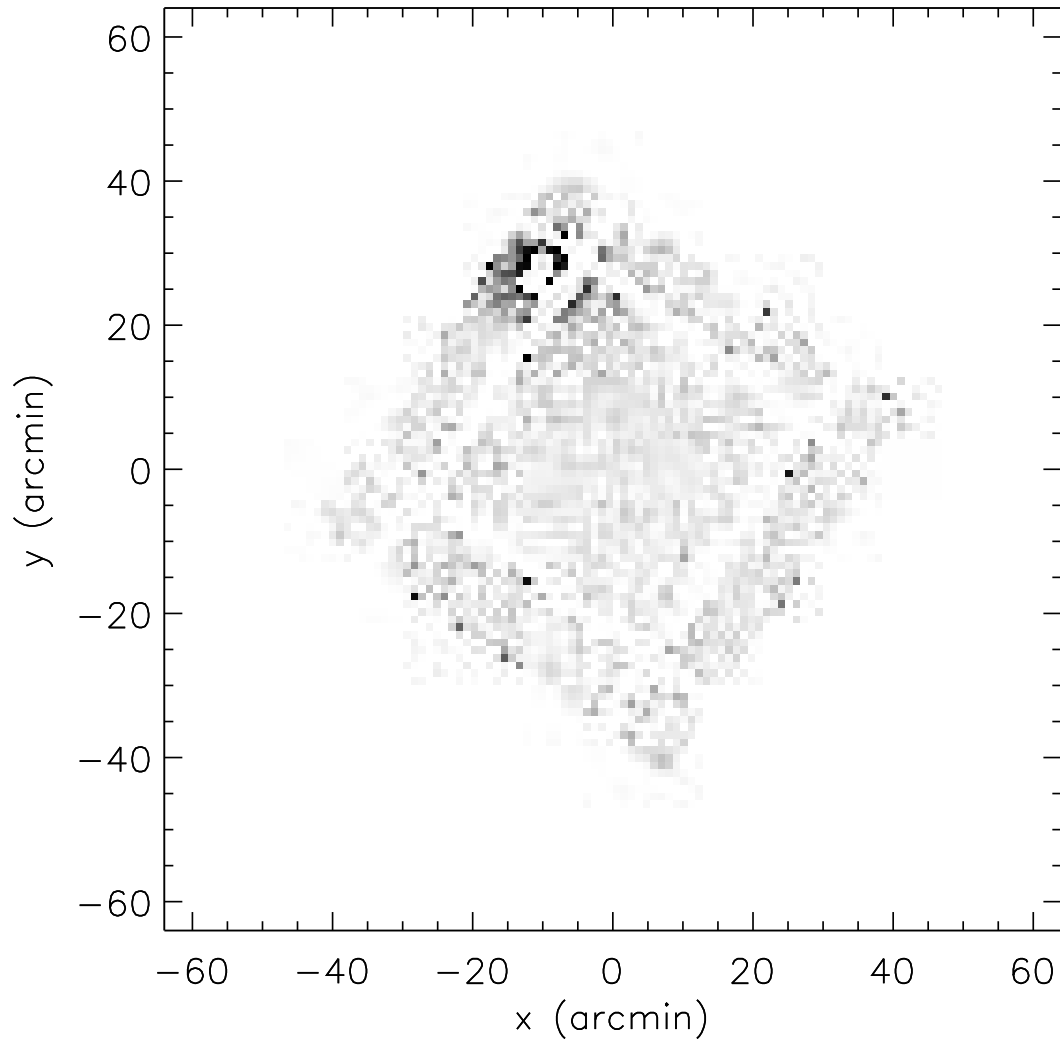


Fig. 7.— Field with sequence number 8926. For clarity, the .81-3.5 keV XRB intensity (a) and the distribution of galaxies with $13.5 < E < 19.0$ (b) are shown separately. This field has the highest non-zero lag correlation in our data set. A cluster of galaxies is visible in the upper left-hand corner.

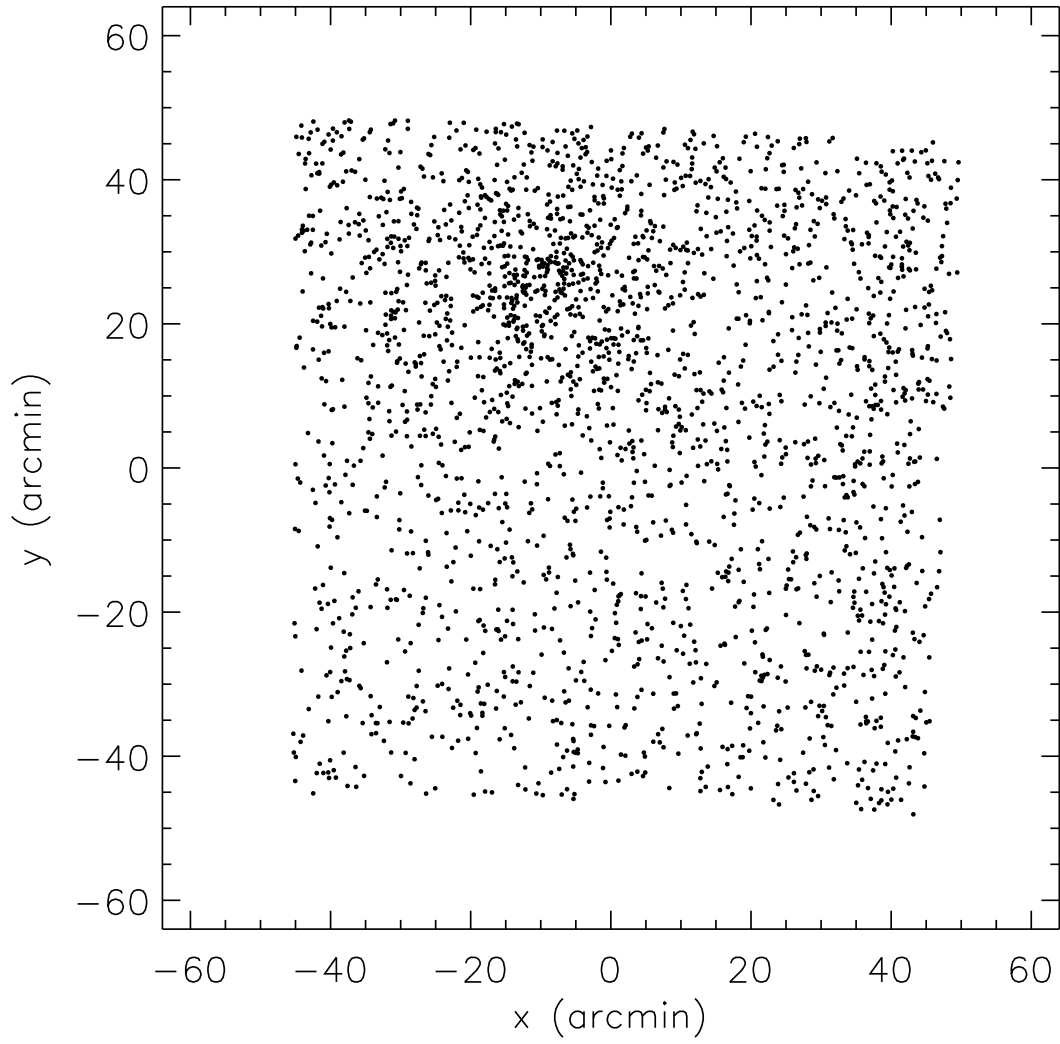


Fig. 7b.—

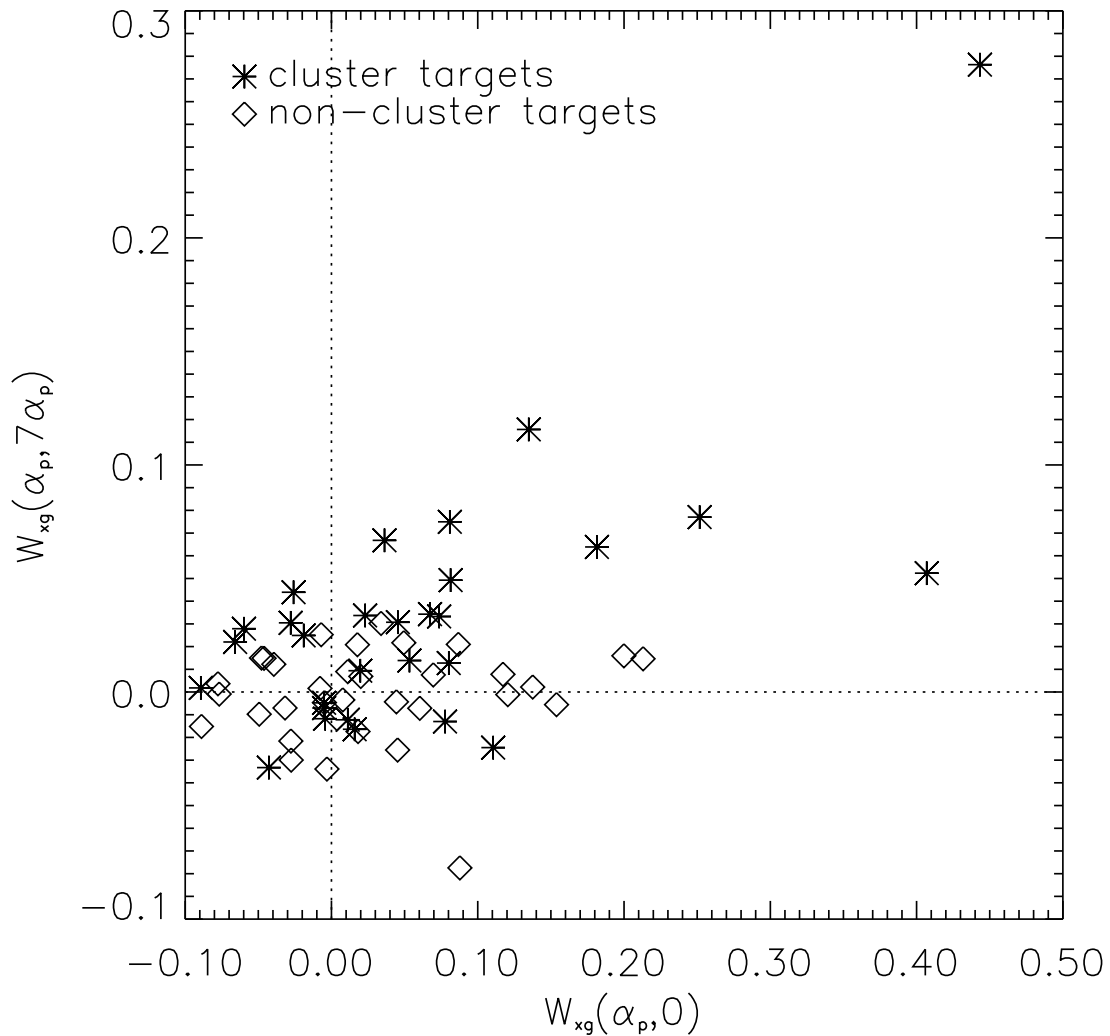


Fig. 8.— Zero-lag vs. Non-zero lag values of W_{xg} for each field. $W_{xg}(\alpha_p, 7\alpha_p)$ is taken as representative of the non-zero lag value. Fields with clusters and non-cluster *Einstein* targets are displayed as stars and diamonds, respectively.

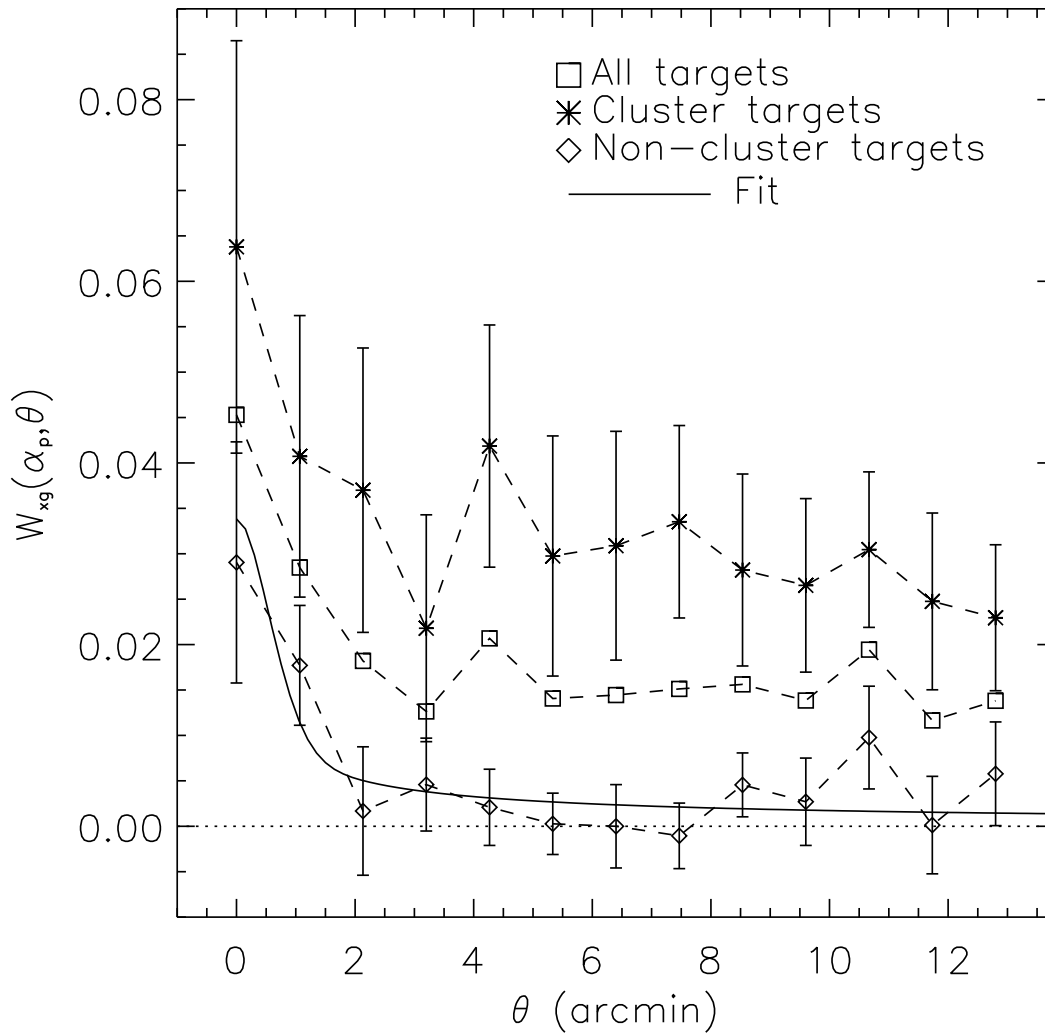


Fig. 9.— Non-zero lag results for cluster and non-cluster targets separately. The value of W_{xg} for all fields combined is redisplayed for comparison. The solid line is the best fit of the Poisson + clustering terms to the non-cluster target field values.

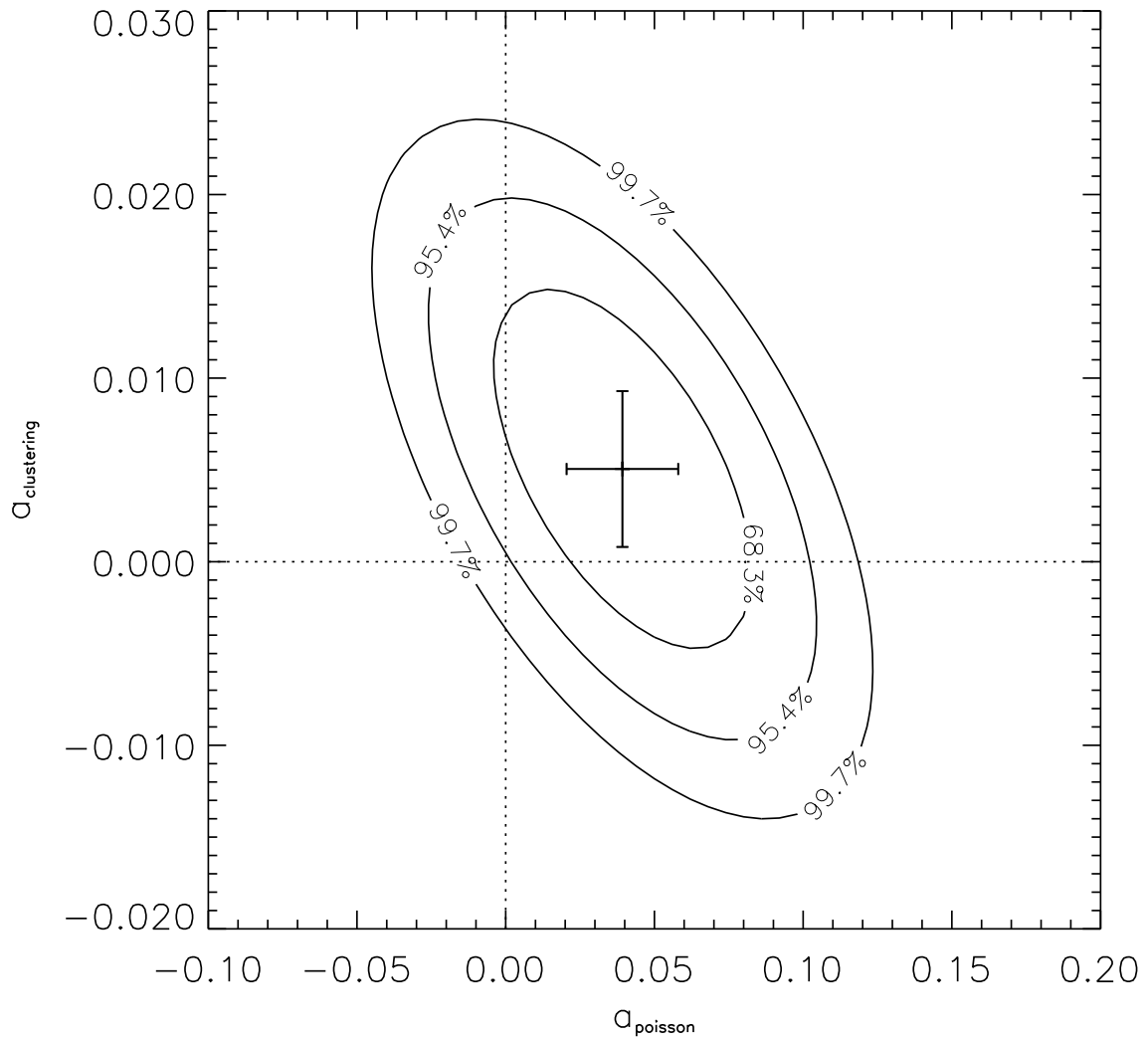


Fig. 10.— Confidence contours for the fit of the Poisson + clustering terms to the non-cluster fields values of $W_{xg}(\alpha_p, \theta)$. The best fit parameters and their associated error bars are displayed as the cross.

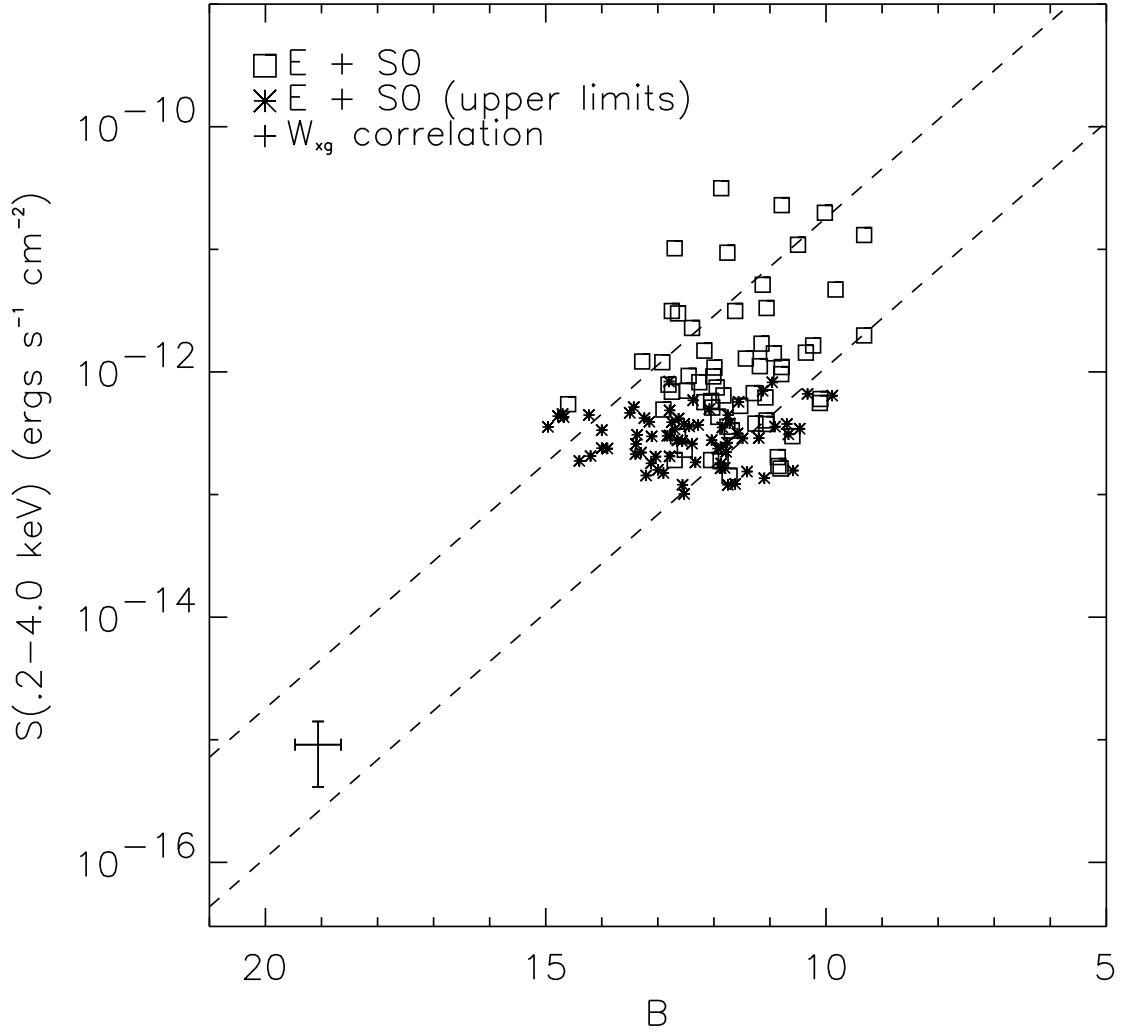


Fig. 11.— Apparent B-magnitudes and X-ray fluxes for the galaxies in the catalog of Fabbiano et al. (1992). The values are shown separately for: (a) Spirals and Irregulars, and (b) Ellipticals and S0s. The dashed lines correspond to the 1σ limits for each of these types of galaxies, assuming a constant X-ray-to-optical flux ratio. The value of the mean galaxy flux derived from our cross-correlation analysis is indicated as the cross.

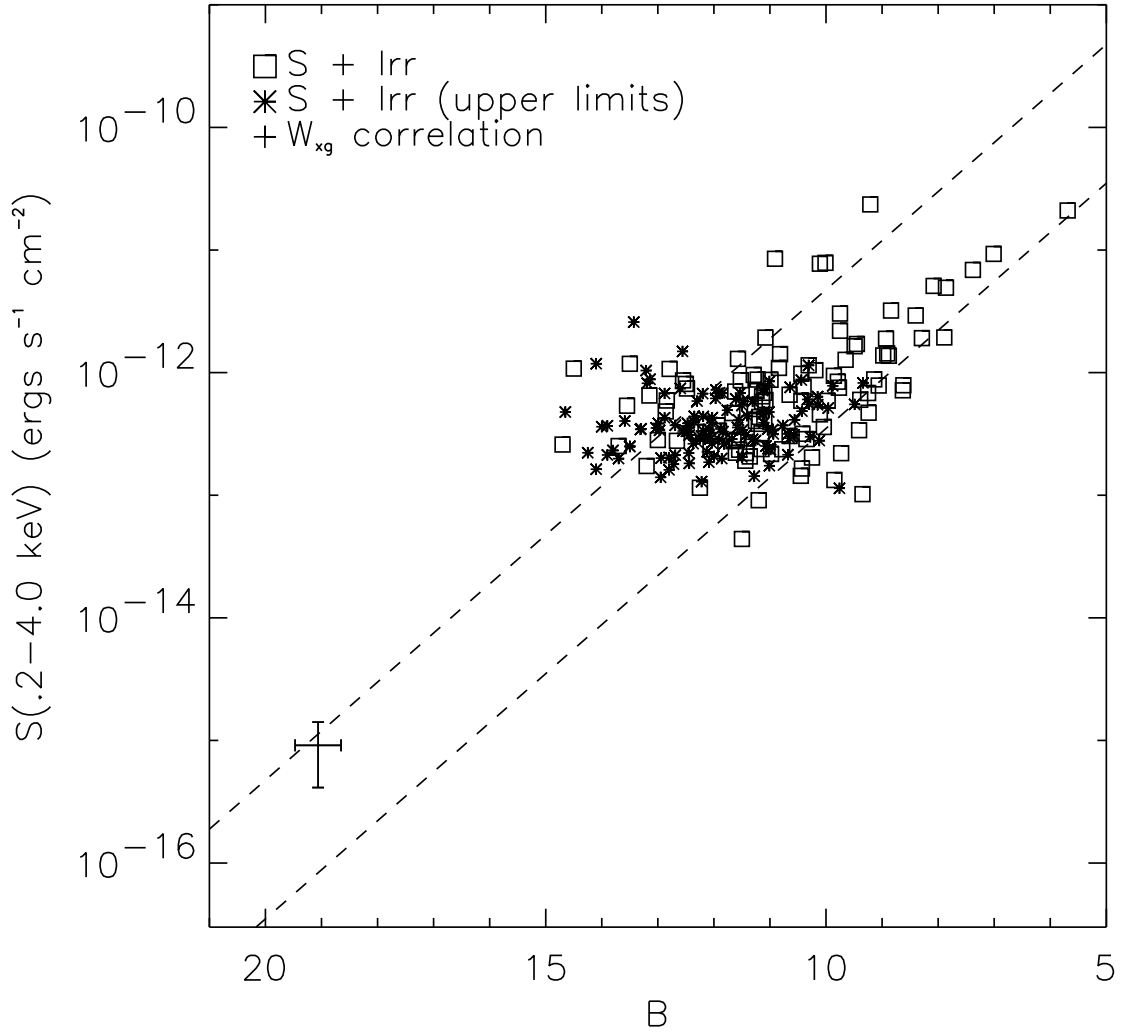


Fig. 11b.—

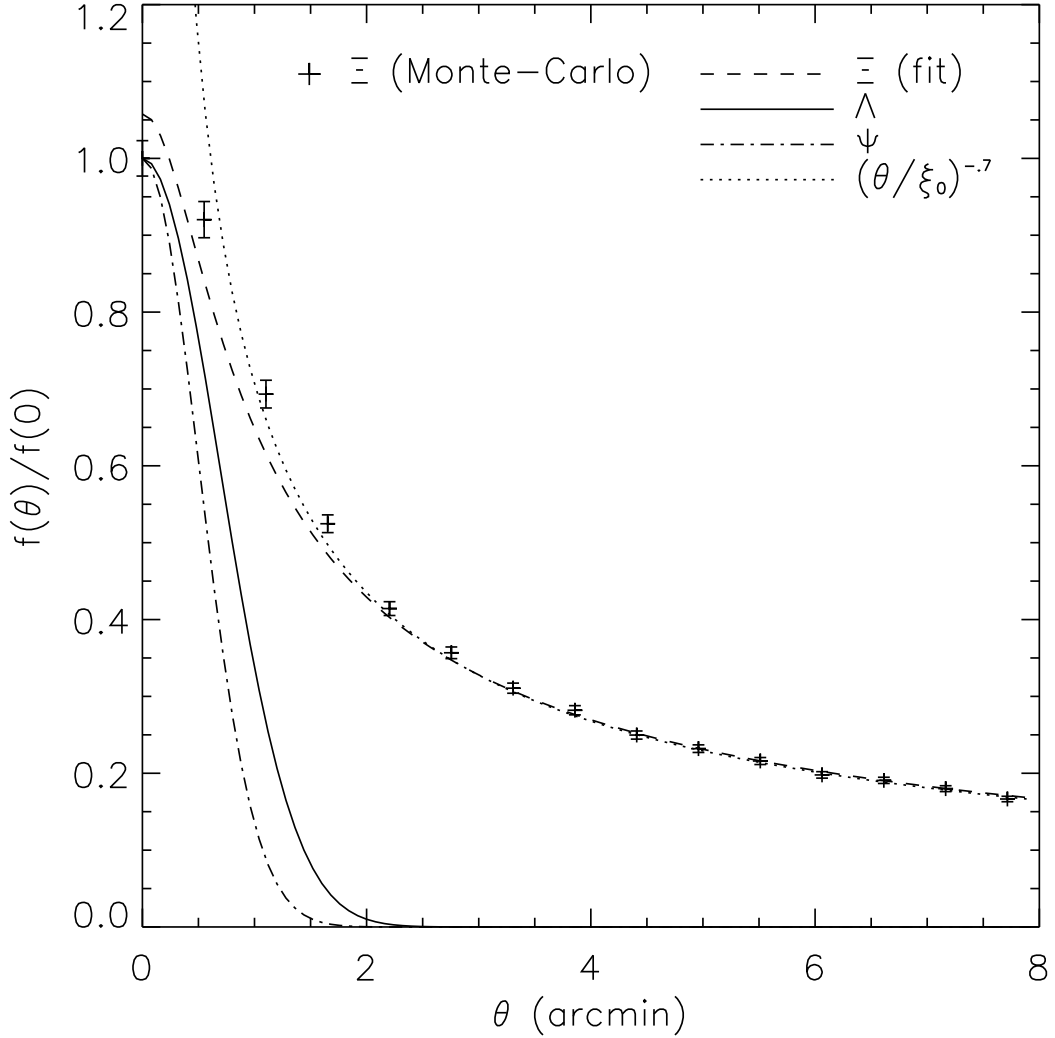


Fig. 12.— Functions used in the interpretation of W_{xg} for parameters relevant to our study, i.e. for $\alpha = \alpha_p = 64''$, $\sigma = \sigma_{psf} = .5'$, and $\beta = .7$. The dot-dashed curve is the PSF. The solid curve is $\Lambda(\alpha, \sigma, \theta)$. The crosses are the result of the Monte-Carlo evaluation of $\Xi(\alpha, \sigma, \beta, \theta)$ with error bars corresponding to 2σ limits. The dashed curve is the analytic function used to model Ξ . For comparison, the asymptotic form $(\theta/\xi_0)^{-\beta}$ is displayed as the dotted line. All functions have been normalized to one at $\theta = 0$. The actual normalizations are $\Lambda(0) \simeq .551$ and $\Xi(0) \simeq 1.480$.

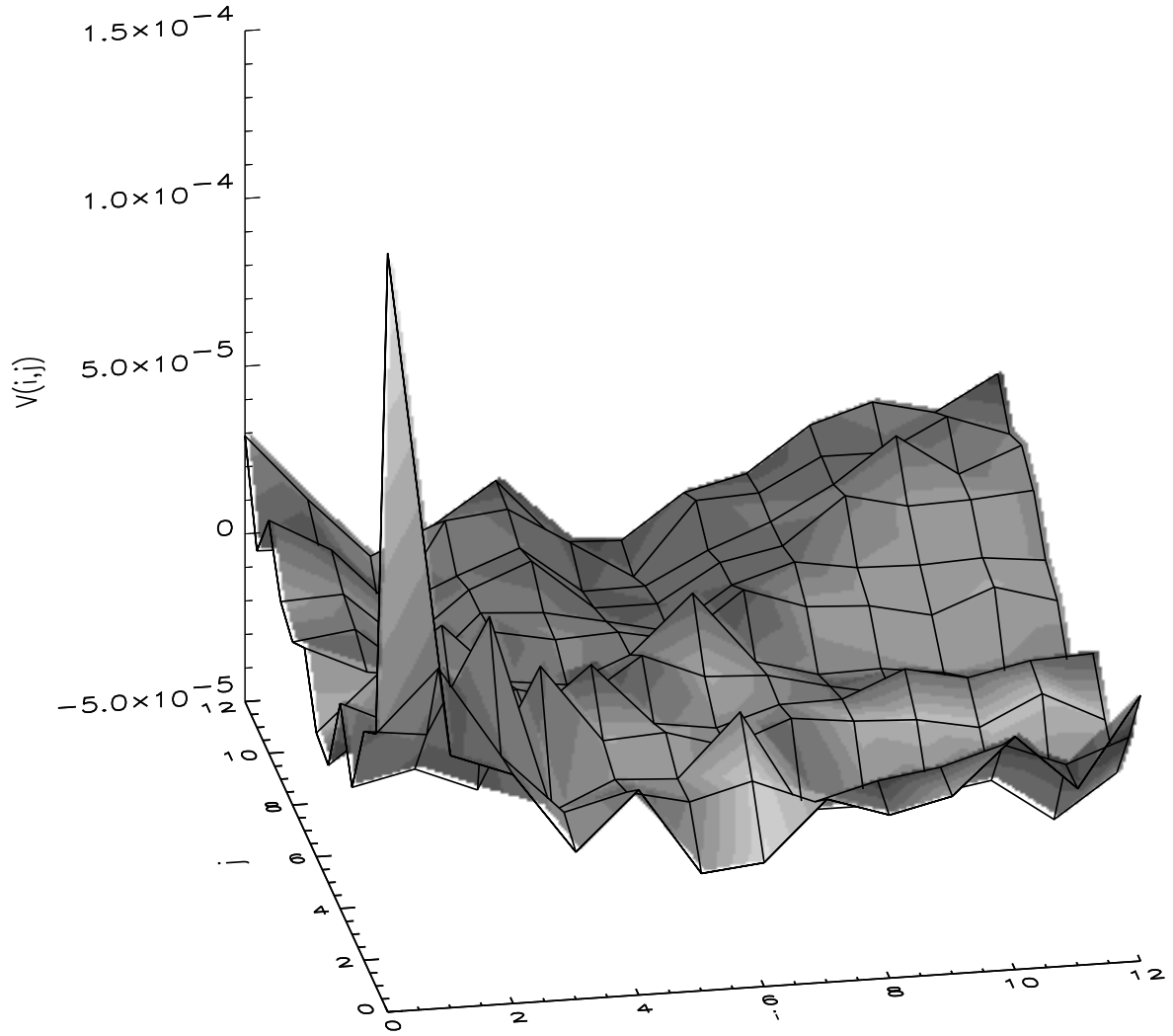


Fig. 13.— Covariance $V(i, j)$ of $W_i \equiv W_{xg}(\alpha_p, \theta_i)$. The indices i and j correspond to θ/α_p .